LJMU Research Online

Hinds, KR, Perley, DA, Sollerman, J, Miller, AA, Fremling, C, Moriya, TJ, Das, KK, Qin, YJ, Bellm, EC, Chen, TX, Coughlin, M, Jacobson-Galán, WV, Kasliwal, M, Kulkarni, S, Masci, FJ, Mahabal, AA, Pessi, PJ, Purdum, J, Riddle, R, Singh, A, Smith, R and Sravan, N

 Inferring CSM properties of Type II SNe using a magnitude-limited ZTF sample

https://researchonline.ljmu.ac.uk/id/eprint/27038/

Article

For more information please contact researchonline@ljmu.ac.uk

Inferring CSM properties of Type II SNe using a magnitude-limited ZTF sample

K-Ryan Hinds [1]⋆ Daniel A. Perley [1] Jesper Sollerman [2] Adam A. Miller [3,4]
Christoffer Fremling,[5,6] Takashi J. Moriya [7,8,9] Kaustav K. Das,[10] Yu-Jing Qin [10] Eric C. Bellm,[11]
Tracy X. Chen,[12] Michael Coughlin [13] Wynn V. Jacobson-Galán [10]† Mansi Kasliwal [10]
Shri Kulkarni,[10] Frank J. Masci,[12] Ashish A. Mahabal [6,14] Priscila J. Pessi [2] Josiah Purdum,[5]
Reed Riddle [5] Avinash Singh,[2] Roger Smith[5] and Niharika Sravan[15]

[1]*Astrophysics Research Institute, Liverpool John Moores University, 146 Brownlow Hill, Liverpool L3 5RF, UK*
[2]*Department of Astronomy, The Oskar Klein Center, Stockholm University, AlbaNova University Center, SE 106 91 Stockholm, Sweden*
[3]*Center for Interdisciplinary Exploration and Research in Astrophysics and Department of Physics and Astronomy, Northwestern University, 1800 Sherman Ave, Evanston, IL 60201, USA*
[4]*NSF – Simons AI Institute for the Sky (SkAI), 172 E. Chestnut St., Chicago, IL 60611, USA*
[5]*Caltech Optical Observatories, California Institute of Technology, Pasadena, CA 91125, USA*
[6]*Division of Physics, Mathematics and Astronomy, California Institute of Technology, Pasadena, CA 91125, USA*
[7]*National Astronomical Observatory of Japan, National Institutes of Natural Sciences, 2-21-1 Osawa, Mitaka, Tokyo 181-8588, Japan*
[8]*Department of Advanced Studie, Graduate Institute for Advanced Studies, SOKENDAI, 2-21-1 Osawa, Mitaka, Tokyo 181-8588, Japan*
[9]*School of Physics and Astronomy, Monash University, Clayton, VIC 3800, Australia*
[10]*Department of Astronomy and Astrophysics, Cahill Center for Astrophysics, California Institute of Technology, MC 249-17, 1200 E California Boulevard, Pasadena, CA 91125, USA*
[11]*DIRAC Institute, Department of Astronomy, University of Washington, 3910 15th Avenue NE, Seattle, WA 98195, USA*
[12]*IPAC, California Institute of Technology, 1200 E. California Blvd, Pasadena, CA 91125, USA*
[13]*School of Physics and Astronomy, University of Minnesota, Minneapolis, MN 55455, USA*
[14]*Center for Data Driven Discovery, California Institute of Technology, Pasadena, CA 91125, USA*
[15]*Department of Physics, Drexel University, Philadelphia, PA 19104, USA*

ABSTRACT

Although all Type II supernovae (SNe) originate from massive stars possessing a hydrogen-rich envelope, their light-curve morphology is diverse, reflecting poorly characterized heterogeneity in the physical properties of their progenitor systems. Here, we present a detailed light-curve analysis of a magnitude-limited sample of 639 Type II SNe from the Zwicky Transient Facility Bright Transient Survey. Using Gaussian processes, we systematically measure empirical light-curve features (e.g. rise times, peak colours, and luminosities) in a robust sampling-independent manner. We focus on rise times as they are highly sensitive to pre-explosion progenitor properties, especially the presence of a dense circumstellar medium (CSM) shed by the progenitor in the years immediately pre-explosion. By correlating our feature measurements with physical parameters from an extensive grid of STELLA hydrodynamical models with varying progenitor properties (CSM structure, $\dot{M}$, R_{CSM}, and M_{ZAMS}), we quantify the proportion of events with sufficient pre-explosion mass loss to significantly alter the initial light curve (roughly $M_{CSM} \geq 10^{-2.5}\,M_{\odot}$) in a highly complete sample of 377 spectroscopically classified Type II SNe. We find that 67 ± 6 per cent of observed SNe in our magnitude-limited sample show evidence for substantial CSM ($M_{CSM} \geq 10^{-2.5}M_{\odot}$) close to the progenitor ($R_{CSM} < 10^{15}$ cm) at the time of explosion. After applying a volumetric-correction, we find 36^{+5}_{-7} per cent of all Type II SN progenitors possess substantial CSM within 10^{15} cm at the time of explosion. This high fraction of progenitors with dense CSM, supported by photometric and spectroscopic evidence of previous SNe, reveals mass-loss rates significantly exceeding those measured in local group red supergiants or predicted by current theoretical models.

Key words: stars: mass-loss – transients: supernovae.

1 INTRODUCTION

Light curves of core-collapse supernovae (CCSNe), Type II SNe in particular, exhibit a large amount of diversity, varying across orders of magnitude in rise times, luminosities, and durations. The

⋆ E-mail: K.C.Hinds@2021.ljmu.ac.uk
† NASA Hubble Fellow

simple progenitor scenario, in which the initial mass is the only factor affecting the SN type or its light curve, cannot adequately explain the extensive observational diversity we see in photometry and spectroscopy – particularly with the acknowledgement of the role binarity plays in stellar evolution (e.g. Eldridge, Izzard & Tout 2008; Sana et al. 2012; Eldridge et al. 2018; Zapartas et al. 2019, 2021) via binary induced mass transfer and mergers.

An area being explored in greater detail is the degree to which diversity arises from stars with similar initial masses and evolutionary histories that, none the less, produce distinct observational signatures at the time of explosion; e.g. varying mass of H envelopes, progenitor radii, and H-richness of the outer envelope (e.g. Popov 1993; Chieffi et al. 2003; Young 2004; Humphreys et al. 2020; Reynolds et al. 2020; Hiramatsu et al. 2021; Dessart & Jacobson-Galán 2023; Moriya et al. 2023b). Type II SNe result from the core-collapse of stars with initial masses between 8–20 $M_\odot$ (e.g. Eldridge & Tout 2004; Smartt 2009, 2015; Van Dyk 2017; Beasor et al. 2020). The most common subtype, Type IIP, originate from red supergiants (RSGs) – a connection confirmed through pre-explosion *Hubble Space Telescope* imaging (see Smartt 2009, 2015). Their light curves exhibit H-recombination powered ∼100 d plateaus following steep rises to peak brightness, typically occurring within days to a week (e.g. Langer 2012; Anderson et al. 2014; González-Gaitán et al. 2015; Rubin et al. 2016; Valenti et al. 2016).

Less common hydrogen-rich subtypes include: Type IIb SNe showing H-to-He spectral evolution from thin H envelopes (Podsiad-lowski et al. 1993; Benson et al. 1994; Woosley et al. 1994; Jerkstrand et al. 2014); Type IIn SNe with slower rises and narrow emission lines from circumstellar material (CSM) interactions (Schlegel 1990; Mauron & Josselin 2011; Smith 2014; Arcavi 2017); and SN 1987A-like events from blue supergiants with extended >30 d nickel-powered rises (Schaeffer et al. 1988; Woosley 1988; Arnett et al. 1989; Schlegel 1990; Suntzeff & Bouchet 1990; Arcavi 2017; Singh et al. 2019; Sit et al. 2023).

From the emergence of narrow emission lines in early spectra of young SNe (flash ionization; Gal-Yam et al. 2014; Groh 2014; Gal-Yam 2017; Yaron et al. 2017; Bruch et al. 2023), strong evidence has been presented for the presence of a substantial mass of dense material close to the progenitor at the time of core-collapse. Narrow lines are likely the result of shock breakout (SBO) shock-heating and ionizing a slow-moving, dense material (e.g. Yaron et al. 2017; Irani et al. 2024; Jacobson-Galán et al. 2024a). As the narrow lines typically persist for only a ∼ few days post-explosion, it is assumed that the CSM required is the result of mass loss from the star in the years immediately preceding core-collapse (e.g. Das & Ray 2017; Davies, Plez & Petrault 2022; Tinyanont et al. 2022; Pearson et al. 2023).

Measurements of the CSM properties from the flash ionization allow for constraints on the mass-loss rate, $\dot{M}$, and late-stage RSG instabilities experienced in the centuries-decades-years immediately before core-collapse (e.g. Mauron & Josselin 2011; Yaron et al. 2017; Morozova, Piro & Valenti 2018; Bruch et al. 2021; Stroh et al. 2021; Tinyanont et al. 2022; Bruch et al. 2023; Moriya et al. 2023b; Pearson et al. 2023). These analyses typically assume that the CSM is an unbound, spherically symmetric material escaping with velocities of order ∼10–100 km s^{-1} (Smith 2014; Morozova, Piro & Valenti 2017), following a density profile that decreases with radius ($\rho \propto r^{-2}$ for steady-state mass loss, Moriya et al. 2018, 2023b; Morozova et al. 2018; Davies et al. 2022). Bruch et al. (2021, 2023) find that ∼ 60 per cent of Type II SNe show evidence for significant amounts of dense CSM confined to a region around the progenitor at the time of explosion – although, this figure is not corrected for observational biases and not volume limited. Potential precursor

events (e.g. Fraser et al. 2013; Jacobson-Galán et al. 2022; Dong et al. 2024; Warwick et al. 2025) provide further evidence of eruptions close to the 'classical' core-collapse event.

The notion that many Type IIP SNe progenitors are surrounded by dense CSM at the time of explosion is further supported by detailed studies of nearby events: SN 2021yja (≈23 Mpc; Hosseinzadeh et al. 2022; Kozyreva et al. 2022), SN 2023ixf (≈7 Mpc; Bostroem et al. 2023; Hiramatsu et al. 2023; Hosseinzadeh et al. 2023; Jacobson-Galán et al. 2023; Jencson et al. 2023; Li et al. 2024; Singh et al. 2024; Zimmerman et al. 2024), and SN 2024ggi (≈7 Mpc; Chen et al. 2024, 2025; Pessi et al. 2024; Shrestha et al. 2024; Xiang et al. 2024; Jacobson-Galán et al. 2024b), which, combined with early photometric and spectroscopic data, confirm CSM around their RSG progenitors. In these cases, dense, optically thick CSM causes the SBO to occur within the CSM rather than at the stellar surface (Förster et al. 2018; Tinyanont et al. 2022; Pearson et al. 2023), producing rapid rises and enhanced peak luminosities (e.g. Moriya et al. 2011, 2023b; Das & Ray 2017; Morozova et al. 2017, 2018; Bruch et al. 2021, 2023; Tinyanont et al. 2022; Pearson et al. 2023; Li et al. 2024).

$\dot{M}$ for RSGs have been measured through multiple techniques: mid-IR observations of circumstellar dust in clusters show $\dot{M} \sim 10^{-6}$–10^{-5} $M_\odot$yr^{-1} (e.g. Beasor & Davies 2018; Beasor et al. 2020), consistent with rates derived from molecular line and radio measurements (e.g. Mauron & Josselin 2011) and comparing pre-explosion progenitor properties to theoretical stellar evolution models (e.g. Smartt 2009). Type IIn progenitors exhibit much higher rates of 10^{-3}–1 $M_\odot$yr^{-1}, derived from multiwavelength observations (e.g. Kiewe et al. 2012; Taddia et al. 2013; Fransson et al. 2014), and combined X-ray, radio, and spectroscopic signatures (e.g. Smith 2017a, b).

However, $\dot{M}$ inferred from RSG observations alone are insufficient to produce the measured M_{CSM} and R_{CSM} on the time-scale of decades to months pre-explosion (e.g. Bruch et al. 2021, 2023). Popular mechanisms for end-of-life mass-loss include: wave-driven energy heating into the stellar envelope (e.g. Fuller 2017; Morozova et al. 2020; Wu & Fuller 2021), radiation-driven mass-loss (e.g. Vink 2008; Vink & Gautham 2023), instabilities caused by explosive shell burning (e.g. Arnett & Meakin 2011; Smith & Arnett 2014), common envelope interactions caused by binary interactions (e.g. Chevalier 2012; Sana et al. 2012), and RSG 'superwinds' (e.g. Davies et al. 2022).

Previous studies have been successful in characterizing smaller subsets of Type II SN properties such as luminosities and rise times (e.g. Taddia et al. 2013; Anderson et al. 2014; Gall et al. 2015; Sanders et al. 2015; Rubin et al. 2016; Valenti et al. 2016; Graur et al. 2017; Davis et al. 2019) but are limited to small numbers or incomplete samples, made up of well-observed SNe detected in heterogeneous galaxy-targeted surveys. Infrequent and inconsistent survey cadence lead to inadequate coverage on the rise, limiting the amount of information one can infer from the rising light curve. The wide area, high cadences, and untargeted nature of modern surveys allow for larger, more complete samples to be curated – lending to more detailed statistical analysis of population characteristics and their frequencies. This work builds upon previous studies by making use of robust statistical methods and large, highly complete surveys.

To address these questions, we present detailed light-curve analysis of spectroscopically classified Type II SNe from the Zwicky Transient Facility (ZTF; Graham et al. 2019; Masci et al. 2019; Bellm et al. 2019a, b; Dekany et al. 2020). In Section 2, we introduce our sample, present the forced photometry light curves and the Gaussian process (GP) methodology, and data analysis processes used in this

work. We present the sample in Section 3 and explore the diversity of Type II SNe. In Section 4, we empirically infer progenitor properties using a correlation-based analysis based on previous studies. In Section 5, we present the volume corrected (V_{max} method; Schmidt 1968) distributions for M_{CSM}, R_{CSM}, and $\dot{M}$. We then analyse and discuss the implications in Section 6.

Throughout the paper, we correct for Galactic extinction using the NASA Extragalactic Database (NED) extinction tool (using the dust map from Schlafly & Finkbeiner 2011). We assume a cosmological model with $\Omega_M = 0.3$, $\Omega_\Lambda = 0.7$, and $h = 0.7$.

2 METHODS I – SAMPLE, FORCED PHOTOMETRY, AND LIGHT-CURVE MODELLING

2.1 The Zwicky Transient Facility and The Bright Transient Survey

Of the total observing time available to ZTF, a major fraction has been devoted to public surveys – 40 per cent in the initial 2.5 yr, and 50 per cent in subsequent phases. Most of this public observing time is used for a Northern Sky Survey (NSS) of fields above declination $-30°$ in ZTF g and r bands (Bellm et al. 2019b). The NSS began as a 3 d cadence survey and now runs at 2 d cadence. The public surveys generate alerts which are distributed to various community alert brokers (Patterson et al. 2019). ZTF i-band observations are available for some fields which overlap partnership surveys.

The Bright Transient Survey (BTS), described in Fremling et al. (2020), Perley et al. (2020), and Qin et al. (in preparation), is a magnitude-limited survey aiming to spectroscopically classify all extragalactic transients in the Northern hemisphere, satisfying a few basic conditions: a peak apparent magnitude, m_{peak}, ≤ 18.5 mag, visibility from Palomar, and a location out outside of the Galactic plane. As of 2024 December 31, the BTS catalogue includes $> 10\,000$ classified SNe brighter than 19 mag; spectroscopic classification is 95.5 per cent complete down to 18.5 mag for events passing visibility and cadence criteria (see Perley et al. 2020, for a review).[1] The 2–3 d or less cadence and sensitive nature of the survey are required to adequately sample enough of the rise to constrain it with some certainty, and secure detections during the early phase of the light curve, close to the explosion time.

Final classifications (used here), volumetric rates, and luminosity functions from the BTS sample will be presented in the upcoming paper Qin et al. (in preparation) which covers the period starting 2018 to the end of 2024. Both Qin et al. (in preparation) and this work have made use of ZTF observing time, instruments, and software: spectral energy distribution machine (SEDM; Blagorodnova et al. 2018; Rigault et al. 2019; Kim et al. 2022), the DouBle Spectrograph (Oke & Gunn 1982), Global Relay of Observatories Watching Transients Happen Marshal (Kasliwal et al. 2019), and the Fritz SkyPortal Marshal (Duev et al. 2019; van der Walt, Crellin-Quick & Bloom 2019; Duev & van der Walt 2021; Coughlin et al. 2023).

This study analyses the spectroscopically classified SNe from the BTS database,[2] incorporating both BTS classifications and TNS reports archived in the BTS from 2018 May 1 to 2023 December

31, retrieved via the BTS internal Sample Explorer.[3] Beyond the apparent magnitude threshold, Palomar visibility constraints, and Galactic plane exclusion previously discussed, the BTS requires: sufficient temporal coverage spanning 7.5–16.5 d pre-peak to 16.5–28.5 d post-peak, with multiple observations near peak brightness; spectroscopic accessibility up to 30 d post-peak; the transient must be absent in the reference image; and alerts to pass the BTS alert stream filtering criteria detailed in Perley et al. (2020).

The quality cuts ensure light curves are sampled during the rise to peak and well after peak, and are generally independent of light-curve properties. Key values drawn from the sample that are used to comment on demographics have the additional criterion of light curves peaking brighter than 18.5 mag. From hereon, Type II SNe refer to SNe spectroscopically classified as Type II or Type IIP and do not include Type IIn or Type IIb, which are referred to as such.

2.2 Forced photometry light-curve analysis

The ZTF real-time data stream operates by producing alert packets, where an alert is generated based on real-time and historical contextual information (Masci et al. 2019). Point source function (PSF) photometry and difference imaging using ZTF archives generate upwards of $100\,000$ alerts nightly. Photometric measurements are performed based on image-subtracted photometry (ZOGY; Zackay, Ofek & Gal-Yam 2016). The distributed alert packets do not allow for measurements below the detection threshold and do not fix the position, creating room to miss detections if the software does not recover an alert.

Photometry for this study is produced using the ZTF forced photometry service (fps; Masci et al. 2023), with post-processing conducted following the procedures in Miller et al. (in preparation). Briefly, the fps estimates the PSF flux at a user-specified location in all ZTF difference images with coverage of the specified position. The flux measurement uses the same PSF model defined by the ZOGY algorithm that is used to perform image subtraction in the production of ZTF real-time alerts. Observations in which the fps pipeline processing produces a flag, typically because the photometric calibration is excessively noisy or the initial image subtraction failed, are excluded from the analysis. The fps flux measurements require a systematic baseline correction, i.e. there is a small constant offset that needs to be removed to make the pre-SN flux measurements consistent with zero flux (see Masci et al. 2023). The baseline is estimated using observations that were obtained > 100 d before maximum and several hundred days after maximum, where the duration after the peak is determined by conservatively assuming the transient is purely powered by radioactive ^{56}Co decay. Following the baseline correction, the uncertainties for the individual flux measurements are adjusted to account for a systematic trend whereby brighter sources have underestimated uncertainties (see Miller et al., in preparation, for further details). As a final output, this post-processing produces a measurement of the transient flux and its uncertainty in units of μJy, including in images where there is no flux detected from the transient. For this study, Public + Partnership + Caltech ZTF data were used.

2.3 Gaussian process regression

CCSN light curves are difficult to model due to the extensive variety in their photometric behaviour. There exist analytical attempts to

---

[1] These statistics are available on the ZTF BTS Homepage: https://sites.astro.caltech.edu/ztf/bts/bts.php.

[2] Finalized in Qin et al. (in preparation).

[3] A public version is available at: https://sites.astro.caltech.edu/ztf/bts/explorer.php.
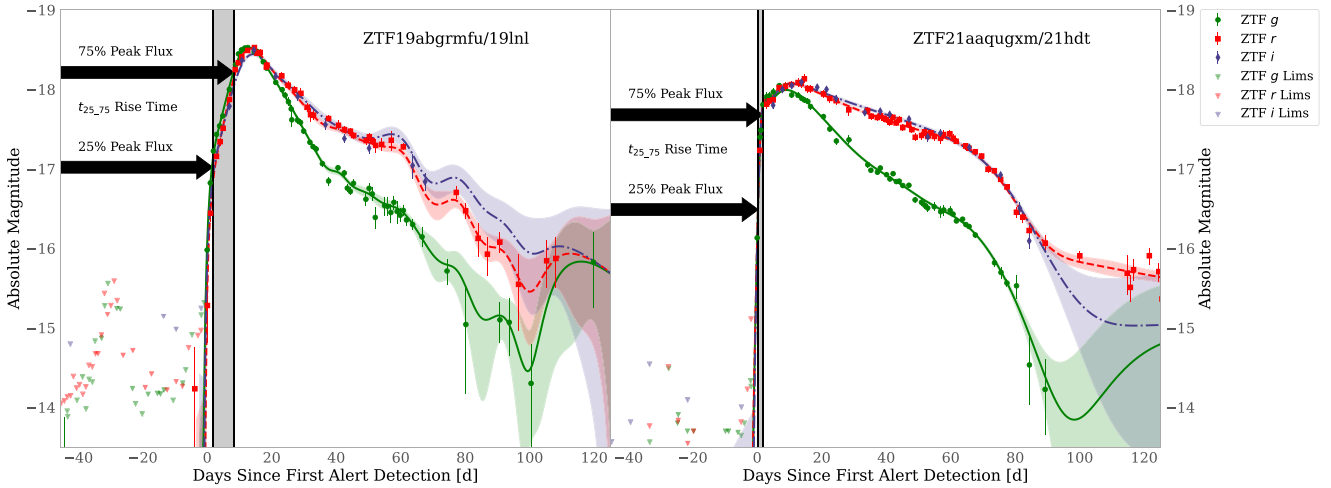
Figure 1. Type II SNe ZTF19abgrmfu/SN 2019lnl at $z = 0.035$ (left) and ZTF21aaqugxm/SN 2021hdt at $z = 0.019$ (right). ZTF gri forced photometry light curve modelled with 2D GPR. We have annotated how a rise time metric (time to rise from 25–75 per cent of the peak flux t_{25_75}) is measured. The inverted triangles represent the upper limits generated by the fps pipeline – where the limit is determined to be the maximum of [flux + $2\times\sigma_{flux}$, $3 \times \sigma_{flux}$]. Circles and the solid line represent ZTF g, squares and the dotted line represent ZTF r, and diamonds and the dash–dotted line represent ZTF i. The shaded regions represent the 68 per cent CI.

address the problem using parametric fitting functions (e.g. Villar et al. 2017, 2019) and there are advancements in theoretical models to produce synthetic light curves with more likeness to observed light curves (Das & Ray 2017; Morozova et al. 2017; Moriya et al. 2023b, and references therein). Whilst certain parametrization and generalized empirical models have proven to be adequate in some scenarios, few of these models can fully characterize the diversity of parameters and properties present in transients being uncovered by large surveys. Thus, we are motivated to use a non-parametric technique such as Gaussian process regression (GPR; Rasmussen et al. 2004).

GPR is a non-parametric, Bayesian machine learning method for modelling data with functions of an unknown form (see Aigrain & Foreman-Mackey 2023, for a review). For single-band SN light-curve interpolation, the unknown function a 1D GP approximates is flux as a function of time. We include the effective wavelength, λ_{eff}, of each filter band, and train in two dimensions – e.g. flux as a function of time and effective wavelength – which is often expressed as probability by equation (1), similar to methodology used in Thornton et al. (2024):

$$P(f|t, \lambda_{eff}) = \mathcal{N}(\mu(t, \lambda_{eff}), \mathbf{K}) \tag{1}$$

where f is flux and λ_{eff} for ZTF g, r, and i is 4753.15, 6369.99, and 7915.49 Å, respectively (Rodrigo & Solano 2020; Rodrigo et al. 2024). The data are input in the observer frame and for plotting purposes, we plot in the observer frame. For parameter measurements (luminosities, time-scales, and colours), we standardize to rest-frame ZTF g by predicting at $\lambda_{eff,g}\times (1 + z)$. This approach allows us to consistently compare physical parameters across our sample, while preserving the original photometric information.

For modelling diverse SN light curves, we use a Matèrn-5/2 covariance function ($\mathbf{K}$) that captures both smooth evolution in addition to the sharp transitions characteristic of SNe – the kernel includes an additive white noise term to account for photometric uncertainties. We implement the GPR using the PYTHON package GEORGE (Ambikasaran et al. 2015), combining the Matèrn-5/2 kernel with the function from Villar et al. (2019) – modified in Sánchez-Sáez et al. (2021), see their equation (A5) – to constrain the behaviour in coverage gaps.

GPR allows robust parameter extraction despite heterogeneous sampling and measurement uncertainties, facilitating empirical correlation analysis without detailed individual modelling. By fitting in flux space, we incorporate non-detections to better constrain early light-curve evolution.

Fig. 1 demonstrates our 2D GPR modelling of ZTF gri light curves for ZTF19abgrmfu/SN 2019lnl and ZTF21aaqugxm/SN 2021hdt. This approach leverages cross-filter correlations to simultaneously predict temporal and spectral evolution – particularly valuable when sampling is irregular across bands. While ZTF g and r observations maintain a regular 2–3 d cadence, ZTF i-band data is often sparse due to partnership-specific scheduling. Our multiband GPR uses well-sampled bands to constrain the less frequently observed ones, enabling more consistent and precise measurements of colour, rise times, and peak magnitudes across all bands.

Our 2D GPR approach uses a single length-scale parameter to handle heterogeneous sampling by controlling correlation strength between observations. While this flexibility accommodates diverse light-curve shapes, it presents challenges: the kernel must balance modelling rapid early evolution with slower late-time decline, potentially overfitting lower signal-to-noise data during the radioactive decay phase. Even with the Villar et al. (2019) function providing a smooth mean function, the GP's flexibility can introduce unphysical variations at late times. The method also assumes consistent colour evolution, potentially misrepresenting rapid colour changes.

However, these limitations primarily affect the faint and late phases, having minimal impact on our scientific conclusions since we focus on bright events ($m_{peak} \leq 18.5$ mag) and measure parameters during well-sampled phases near peak brightness.

2.3.1 Feature extraction

Combining the fps pipeline and GPR developed for this work, we have used 2D GPR to interpolate across all available filters for each SN in the BTS sample, including Type Ia SNe. Using the interpolated light curves and λ_{eff} information, we have empirically measured > 20 metrics (see Table 1) for each band where the coverage allowed for measurements to be reliably taken – for example, coverage

Table 1. Description of parameters empirically measured directly using GPR interpolations (*P1*), or calculated using measured parameters and established relationships – see Section 5.2 for $M_{\rm CSM}$, $\dot{M}$, and $R_{\rm CSM}$. We standardize all measurements by predicting the GP model at $\lambda_{eff} \times (1 + z)$ such that all measurements are in the rest-frame ZTF band or relative to the rest-frame measurements. Most parameters are filter-dependent and have been measured for each filter. The table is split into sections: *P1* are the empirical GP measured parameters used specifically in this work, *P2* are parameters also empirically measured using the GP interpolation but not used in this work, and *P3* which shows parameters estimated from relationships or methods involving parameters in *P1*.

Parameter	Symbol	Unit	Definition
P1 – parameters measured empirically from the GPR model used here			
Peak apparent magnitude	$m_{\rm peak}$	mag	Apparent magnitude at peak [1]
Time of peak	$t_{\rm peak}$	d	Time at which the peak occurs [2]
X–Y per cent rise time	$t_{X,Y}$	d	Time between X per cent and Y per cent of the peak (e.g. 25–75 per cent) [3]
Fade time	$t_{\rm Peak\_50}$	d	E.g. time between peak and 50 per cent peak flux
Duration time	t_{50}	d	E.g. time spent above 50 per cent peak flux
Apparent magnitude at X d	$m_{g,Xd}$	mag	Apparent ZTF g magnitude at 5, 10, and 50 d post-ZTF g peak
Plateau duration	$t_{\rm plat}$	d	Measured using the gradient of the GP interpolated light curve
Colour	$(g-r)_{r,-Xd}$	mag	E.g. ZTF $g-r$ calculated X d before r-band peak
P2 – additional parameters measured empirically from the GPR model not used here			
Plateau colour	$(g-r)_{\rm plat}$	mag	Colour at the end of the plateau
MJD explosion time	$T_{\rm exp}$	d	Explosion time [2]
Colour evolution	$g-r$	mag	ZTF $g-r$ colour relative to ZTF r-band peak
Peak luminosity	$L_{\rm peak}$	erg s^{-1}	Luminosity at peak
Plateau slope	$\nabla_{\rm plat}$	mag d^{-1}	Gradient of the plateau
No. of bumps	$N_{\rm bumps}$	–	The number of peaks in the light curves
Decline rates	Δm_{Xd}	mag d^{-1}	Difference in magnitude between peak and peak + X d
Optical energy	$E_{\rm opt}$	erg	Total integrated optical energy in each band ($\int \nu f_\nu \, d\nu$)
P3 – parameters indirectly measured from relationships involving *P1* parameters			
CSM mass	$M_{\rm CSM}$	$M_\odot$	Mass of circumstellar material
Mass-loss rate	$\dot{M}$	$M_\odot {\rm yr}^{-1}$	Rate of mass loss of the progenitor
CSM radial extent	$R_{\rm CSM}$	cm	Radial extent of circumstellar material
Iron core mass	$M_{\rm Fe, Core}$	$M_\odot$	Iron core mass of progenitor prior to explosion

Notes. [1] Defined as being the peak with the highest flux and it must have previous detections or non-detections on the rise to confirm it is the peak. In the case of multiple peaks, all peaks are identified and the peaks are ranked in order of strength and time (earliest first). All relative time intervals are reported in the rest frame. [2] Relative to first alert detection. [3] We also measure 20–60 per cent, 60–90 per cent, 20–50 per cent, and 50–80 per cent rise times.
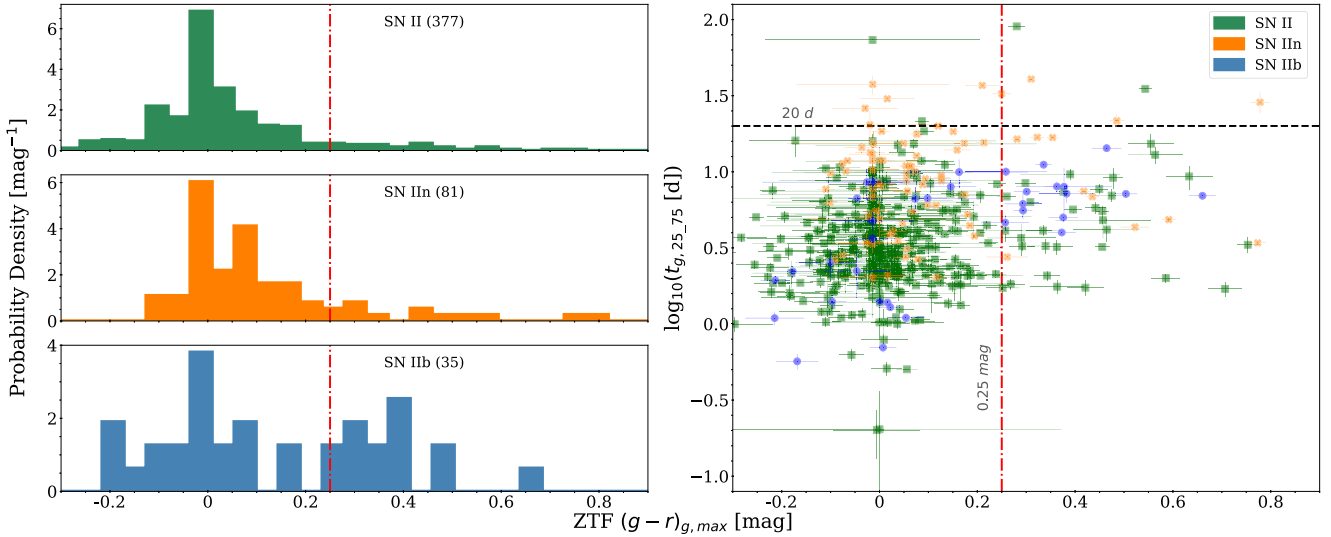
Figure 2. $(g-r)_{g,\mathrm{max}}$ histograms (left) and ZTF g time to rise from 25–75 per cent peak flux versus $(g-r)_{g,\mathrm{max}}$ (right) for Type II, Type IIn, and Type IIb SNe (top left to bottom left) for those with a $m_{\mathrm{peak}} \leq 18.5$ mag in any filter. The histograms for Type II and Type IIn are sharply peaked and have a tail in the red direction indicating a standard colour distribution and the presence of some 'dusty', $(g-r)_{g,\mathrm{max}} \geq 0.25$ mag, SNe. The horizontal line shows 20 d and the vertical line at 0.25 mag is the limit we define, beyond which we identify objects as 'dusty'. This plot is used to distinguish the likely heavily host dust-extinguished SNe (rise < 20 d, and red, $g-r > 0.25$ mag) from those likely intrinsically red (rise $\geq$ 20 d and red, $g-r > 0.25$ mag).

constraints are placed on the rise to ensure reliability, we explore this in more detail in a proceeding section. Metrics relevant for this paper rely first on the peak flux (flux at maximum light) and include: rise times from 10 per cent, 25 per cent, and 50 per cent of the peak flux to the peak flux or 50 per cent, 60 per cent, 75 per cent, 80 per cent, and 90 per cent of the peak flux; the peak flux; magnitude; luminosity; time of the peak relative to the first alert detection; colour at several times before, at and after the peak; plateau length and plateau magnitude; and other metrics for analysis in future works. As mentioned, we standardize these measurements by predicting the GP model for each filter in the rest-frame ZTF band.

We estimate parameter uncertainties by drawing 1000 samples from the GPR posterior distribution, leveraging the probabilistic nature of the GP. The 1σ uncertainties are derived from the resulting distribution of measured values, capturing both photometric uncertainties and the range of light-curve behaviours consistent with our data.

2.4 Galactic and host extinction corrections

We correct for line of sight Galactic extinction using NED extinction tools (based on the dust map from Schlafly & Finkbeiner 2011). For $M_{g,\mathrm{peak}}$ used in this work, we calculate the peak of the GP model, correct for Galactic extinction at the interpolated central wavelength and apply a uniform K-correction of $2.5\log_{10}(1+z)$, which is typically small.

As ZTF is a survey in gri, a comprehensive host extinction correction is not feasible with the survey photometry alone. One can approximately find the host extinction using the ZTF $g-r$ colour at the ZTF g peak, $(g-r)_{g,\mathrm{max}}$, and apply a correction based on this colour. For Type II and Type IIn SNe, we find the unweighted histogram of the peak colour $(g-r)_{g,\mathrm{max}}$, Fig. 2, is sharply peaked around 0 mag, which is characteristic of a well-defined intrinsic population and suggests standard colour distribution, consistent with the findings of de Jaeger et al. (2018).

The Type II SN colour distribution, shown in Fig. 2, has an asymmetric tail toward redder colours. This asymmetry is particularly informative – if there existed a significant population of intrinsically red SNe, we would expect a more symmetric distribution or a secondary peak, rather than the observed sharp core with a red tail. Based on the distribution in Fig. 2, we find the 90th and 95th percentiles for Type II SN $(g-r)_{g,\mathrm{max}}$ to be $\approx$0.2 and $\approx$0.39 mag, respectively. We establish $(g-r)_{g,\mathrm{max}} \geq 0.25$ mag as the threshold for identifying 'dusty' events that necessitate host-extinction correction. Using an empirical cumulative distribution function (ECDF), we find that 9^{+12}_{-6} per cent of the observed Type II population have $(g-r)_{g,\mathrm{max}} \geq 0.25$ mag, confirming that heavily dust-extinguished events constitute a minority of the sample. For Type IIn and Type IIb SNe, we find 14^{+14}_{-8} per cent and 40 ± 20 per cent, respectively, have $(g-r)_{g,\mathrm{max}} \geq 0.25$ mag – uncertainties reported here are the binomial CI.

Using a rise time definition we present in Section 2.5.1, we investigate the rise time versus colour parameter space to understand how this correction is applied to SNe across a variety of rise times – see Fig. 2. The majority of SNe with rise times < 20 d exhibit peak $g-r$ colours blueward of 0.25 mag. Objects redward of this threshold likely suffer significant dust-extinction, forming a skewed tail extending from an otherwise approximately normal colour distribution. Those with $(g-r)_{g,\mathrm{max}} > 0.25$ and rise > 20 d are likely intrinsically red, owing to photons emitted from the core being trapped for longer which increases diffusion time and rise time to maximum light. We perform this exercise to avoid applying an incorrect host correction to those SNe that are likely intrinsically red, therefore artificially boosting their luminosity. As we have identified this population in the top-right quadrant (rise > 20 d and $(g-r)_{g,\mathrm{max}} > 0.25$ mag) as intrinsically red, we correct the subset in the bottom-right quadrant (rise < 20 d and $(g-r)_{g,\mathrm{max}} > 0.25$ mag).

To ensure that our method is accurately identifying events affected by dust extinction (requiring host-extinction corrections), we inspected the host Galaxy environments of the 'dusty' SNe (22 Type II, 8 Type IIn, and 11 Type IIb after 18.5 mag cut for completeness, see Table A1 for a summary of properties). We examined these

environments for indicators that could explain the reddening, such as substantial dust content, location within dense spiral arms, the galactic bulge or edge-on or highly inclined host galaxy orientations. We see that these events are predominantly located in regions associated with significant dust content – specifically within their host galactic plane or star-forming regions. These SNe also show a persistent red colour throughout their rise phase, consistent with dust extinction rather than intrinsic colour variation. This environmental association, combined with their photometric evolution, suggests that their red appearance stems from host galaxy extinction rather than intrinsic properties. We perform our later analysis both with and without host extinction corrections, finding no significant differences in our primary results.

One event in particular, ZTF18acbwaxk/SN 2018hna (Singh et al. 2019; Thévenot 2020; Maund et al. 2021; Tinyanont et al. 2021; Sit et al. 2023; Xiang et al. 2023), is both red and rises slowly with similar light-curve morphology and time-scales to SN 1987A. This SN appears in a face-on dwarf galaxy, the minimal expected host extinction suggests its red colour is intrinsic – for comparison, SN 1987A was $g - r \gtrsim 0.4$ mag at peak. We interpret this as an intrinsically red event and do not apply a host-correction.

We perform a correction for host extinction with the colour at peak, $(g - r)_{g,\max}$, for this subset of SNe described above. Relative to V band ($A_V = 1$ mag) and based on the assumption of a standard Milky Way $R_V = 3.1$ mag (e.g. Cardelli, Clayton & Mathis 1989) reddening law (as implemented in PYTHON EXTINCTION package). We assume an extinction of $A_g/A_V = 1.19$ mag, $A_r/A_V = 0.84$ mag, and $A_i/A_V = 0.61$ mag – we ignore the effect of redshift here. For a ZTF g extinction relative to $(g - r)_{g,\max}$ reddening of 1 mag, we find an extinction of $A_g = 3.37 \ (g - r)_{g,\max}$ mag. For our correction to ZTF g luminosities, we multiply the $(g - r)_{g,\max}$ by 3.37 and apply this to ZTF g magnitudes of all Types. From this point on, we carry through this extinction correction for light curves where $(g - r)_{g,\max} > 0.25$ and $t_{25\_75} \leq 20$ d. However, the volumetric-correction weighting applied in Section 3.2 is based on the uncorrected peak magnitude.

To minimize overweighting low luminosity, nearby events in our magnitude-limited analysis, we adopt more precise luminosity distances from recent literature for events within $d_{l,\max} \leq 50$ Mpc (Table 2).

2.5 Rise time

We focus on the rise time and how it relates to the CSM as recent studies (e.g. Morozova et al. 2016, 2018; Yaron et al. 2017; Hosseinzadeh et al. 2018, 2023; Bruch et al. 2021, 2023; Tinyanont et al. 2022; Jacobson-Galán et al. 2023; Pearson et al. 2023; Irani et al. 2024) have shown substantial evidence of the sensitive nature of the rise time to the progenitor properties and pre-explosion conditions (e.g. M_{CSM}, R_{CSM}, CSM density, and progenitor radius).

Traditional rise time measurements – from explosion to peak – require well-constrained explosion epochs through deep non-detections immediately before explosion and good sampling of the early rise. These observational constraints significantly limit the number of events for which explosion epochs can be reliably determined, though this is partially alleviated by fitting the early light curve with power law or polynomial functions to approximate the explosion time (Gall et al. 2015; González-Gaitán et al. 2015; Bruch et al. 2021, 2023). To analyse our heterogeneously sampled data set, we instead adopt a mathematically defined rise time that does not depend on explosion epoch constraints.

Table 2. Sources of improved luminosity distance for events closer than 50 Mpc to improve the luminosity weighted volumetric-corrections of close events, particularly those at the extremes – close and faint.

ZTF	TNS ID	d_l [Mpc]	Reference
ZTF18acbwaxk	2018hna	12.82 ± 2.02	[1]
ZTF18abwkrbl	2018gjx	35.00 ± 5.00	[2]
ZTF19abwztsb	2019pjs	40.10	[3,4]
ZTF19acfejbj	2019sox	48.78	[5]
ZTF20acrzwvx	2020aatb	40.50 ± 5.11	[4,6]
ZTF20acwqqjs	2020acat	35.30 ± 4.40	[7]
ZTF20aapchqy	2020cxd	22.00 ± 3.00	[8]
ZTF20aatzhhl	2020fqv	17.30 ± 3.60	[9,10]
ZTF20abeohfn	2020mjm	28.30 ± 2.00	[3,4]
ZTF21aadoizf	2021aai	20.90 ± 1.90	[11]
ZTF21aaqgmjt	2021gmj	13.10 ± 2.00	[12]
ZTF21abvcxel	2021wvv	44.12	[5]
ZTF22abtjefa	2022aaad	11.10	[5]
ZTF22abtspsw	2022aagp	21.83 ± 3.00	[4]
ZTF22aaotgrc	2022ngb	43.07	[4]
ZTF22aauurbv	2022pgf	36.63 ± 2.60	[4]
ZTF22abfzdkz	2022uop	44.65	[5]
ZTF22abnejmu	2022ycs	44.65	[5]

Notes. [1]Singh et al. (2019); [2]Prentice et al. (2020); [3]Strotjohann et al. (2021); [4]Helou et al. (1991); [5]NASA/IPAC Extragalactic Database Helou et al. (1991); [6]Theureau et al. (2005); [7]Medler et al. (2022); [8]Yang et al. (2021); [9]Tinyanont et al. (2022); [10] Theureau et al. (2007); [11]Valerin et al. (2022); and [12]Zimmerman et al. (2021).

2.5.1 Rise distribution

We define rise time (t_{25_75}) as the interval from 25 per cent to 75 per cent of peak flux in ZTF g band. This definition offers several advantages: it is robust against sampling errors and low signal-to-nosie (S/N) measurements; captures the epoch where CSM signatures are strongest; and avoids plateau phases where other physical processes dominate. We select ZTF g band for its sensitivity to CSM interaction signatures in the blue optical (e.g. Gal-Yam et al. 2014; Groh 2014; Yaron et al. 2017; Kulkarni et al. 2023) – a choice validated by recent modelling of SN 2023ixf, where g band provided optimal fits (minimum χ^2 per progenitor model) across all bands (Moriya & Singh 2024).

Events peaking at 18.5 mag have 25 per cent peak flux at 20th mag (e.g. $+1.5$ mag), which does not typically exceed the ZTF detection limit under favourable conditions but may fall below the threshold during suboptimal conditions (e.g. bright time). Thus, this ensures we capture a substantial portion of the rise whilst remaining sensitive to fainter objects. Fig. 1 shows our measurement methodology.

For consistent measurements on the rise, we place additional constraints on the rising light curve coverage to minimize the impact large gaps in coverage have on the GP modelling. For the measurement, we required at least one observation (detection or non-detection) in each of the following regions:

(i) $T_{g,75} - 4 \ \leq T \leq T_{g,75} + 4$ [d];
(ii) $T_{g,75} - 12 \leq T \leq T_{g,75} - 4$ [d];
(iii) $T_{g,75} - 20 \leq T \leq T_{g,75} - 12$ [d].

Here, $T_{g,75}$ marks when the flux reaches 75 per cent of its peak during the rising phase in ZTF g. To measure rise times in the ZTF g band, we begin by examining only the g-band data. When ZTF g-band coverage is incomplete (missing regions B and/or C), we expand our analysis to include ZTF r- and i-band data, evaluating them relative to $T_{g,75}$. In cases where ZTF g-band data only covers
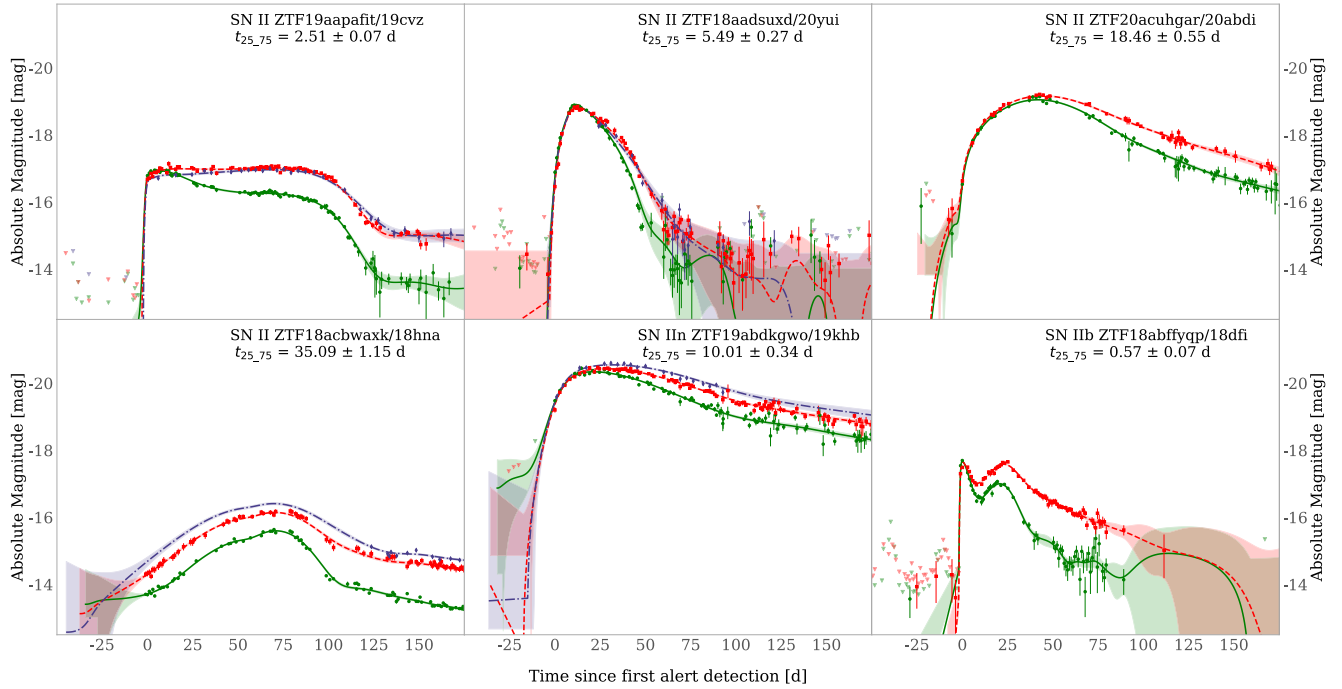
Figure 3. ZTF *gri* forced photometry GPR light-curve panel showing the diversity of Type II SNe and the ZTF *g* t_{25_75} rise times.

region A, we classify the measurement as an upper limit if the ZTF *r* and *i* bands cover either regions A and B together or regions A and C together. For early rise measurements ($T_{b,25}$, time at 25 per cent peak flux relative to ZTF *g*), we require coverage of only region A. This requirement is typically met automatically through our $T_{g,75}$ criteria since most objects complete their rise within 20 d. The diversity of light curve morphologies is shown in Fig. 3.

From our sample of SNe with forced photometry (as of 2023 December 31), we identified 1323 CCSNe that meet the quality criteria established by Perley et al. (2020). Of these, 981 are hydrogen-rich CCSNe (including regular Type II/IIP, IIn, IIb, and H-rich superluminous SNe; SLSNe), while the remaining 342 are classified as stripped-envelope SNe. The other SNe in the quality sample, 4009, are Type Ia SNe (see Table 3). Our Type IIb sample is relatively small due to classification challenges inherent to this subtype. The limited spectral resolution of the SEDM makes it difficult to identify the characteristic evolution – specifically, the disappearance of H features and the emergence of often weak He lines in later spectra. Comprehensive classification typically requires multiple spectra obtained at different epochs, which is not always feasible. While this likely results in some incompleteness in our Type IIb sample, the impact on our overall study conclusions is minimal, as these events represent a small fraction of the H-rich SN population. We discuss and quantify this systematic impact of this in Appendix A10.

Given the coverage constraints and the availability of forced photometry at the time of writing, 639 H-rich SNe make it through our quality cuts, allowing for constraining measurements of the t_{25_75} metric to be made – see Table 3 for a breakdown. For this paper, we consider SLSNe II as Type IIn based on the ambiguous boundary between the classes. Additionally, for the 23 SLSNe passing the quality cuts from the BTS and outlined here, we checked their spectra and found obvious narrow lines indicative of Type IIn SNe in all except ZTF19ackzvdp/SN 2019uba which showed slightly broader emission lines (see also Nyholm et al.

Table 3. Figures showing the number of SNe in the BTS quality sample (see Perley et al. 2020) between the 2018 May 1 and 2023 December 31, in addition to the number of SNe that make up the final sample of this work after applying rise time constraints to ensure an adequate sampling of the rise and a m_{peak} cut for volumetric weighting – m_{peak} can be in any ZTF band.

Type	Total	BTS cut	Rise cut	$m_{peak} \leq 18.5$ mag
H-rich CCSNe				
II/IIP	1387	716	479	377
IIn	241	145	94	71
IIb	136	97	50	35
SL II	38	23	16	10
Tot.	1802	981	639	493
H-poor CCSNe				
Ib/c	363	223	–	–
Ic-BL	63	45	–	–
Ibn	36	27	–	–
Icn	1	1	–	–
SL I	75	46	–	–
Tot.	538	342	–	–
Type Ia SNe				
SN Ia	6329	4009	–	–

2020; Kangas et al. 2022; Pessi et al. 2023), prompting us to exclude this from the sample completely. Fig. 4 is the rise time distribution using t_{25_75} rise including comparison events from the literature.

In Fig. 4, we have included the well-studied Type II SNe SN 2023ixf, SN 2024ggi, and SN 1987A to determine where amongst the larger population these events lie. For SN 2023ixf,[4] and SN 2024ggi,[5]

---

[4]Data gathered from https://www.wiserep.org/object/23278.
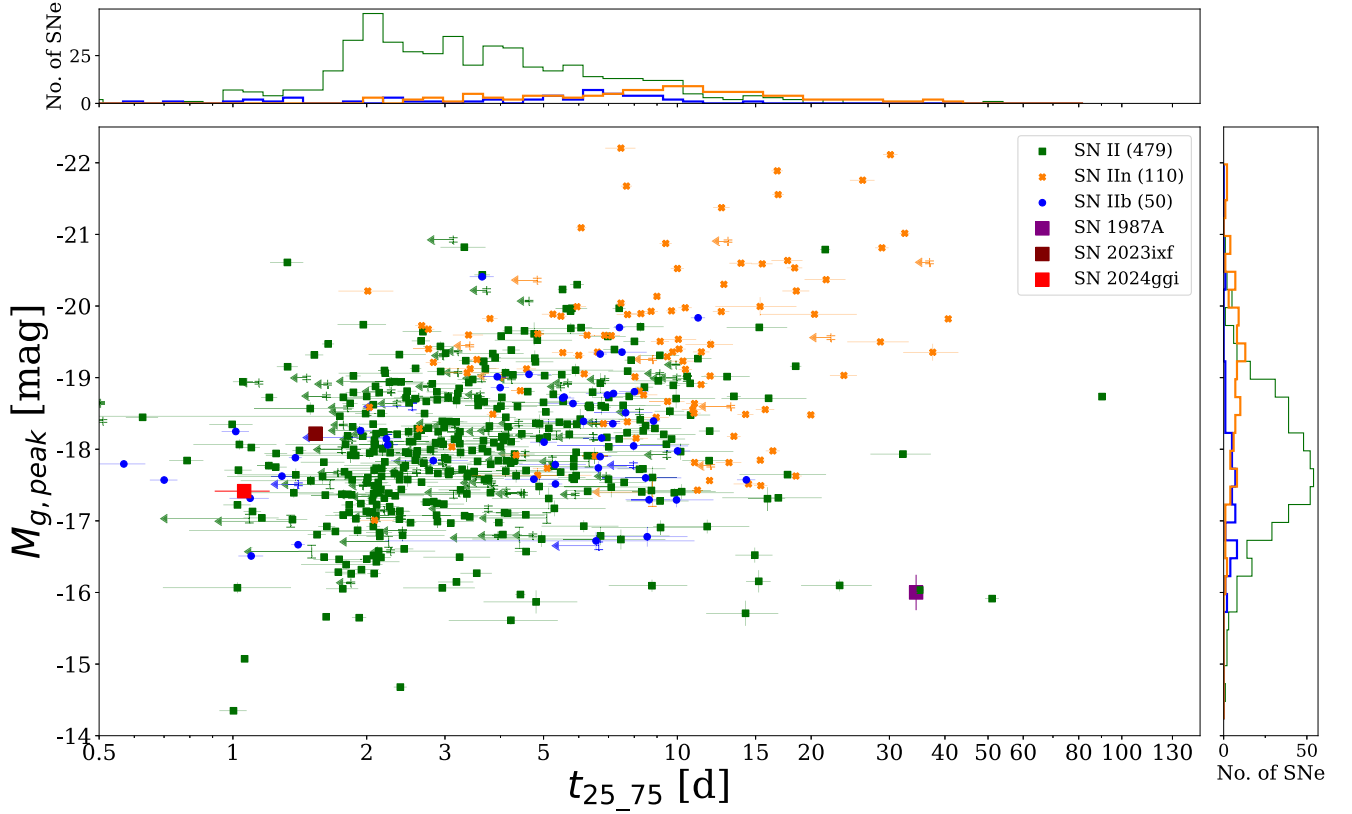[5]Data gathered from Shrestha et al. (2024).

Figure 4. Rise time distribution in ZTF *g* band for spectroscopically classified SNe II, SNe IIn, and SNe IIb. The squares are: SN 1987A (purple and rightmost), the SN 2023ixf (brown and middle), and SN 2024ggi (red and leftmost). Arrows represent upper limits on the rise times as they meet only two of the criteria from Section 2.5.1. These peak magnitudes are corrected for Galactic and host extinction, as described in Section 2.4.

we use publicly available data and model the multiband light curve using the same process as described in Section 2.3, and for SN 1987A, we use figures from Schaeffer et al. (1988), Catchpole (1989), Suntzeff et al. (1992), Suntzeff (1997), and Fransson et al. (2007) to extract the data using a data extractor.[6] As shown in Fig. 4, Type II SNe occupy a large range in this parameter space, highlighting the large diversity present in H-rich CCSNe. The Type IIn SNe are preferentially more luminous and generally longer rising, attributed to their larger and more dense CSM components driving a prolonged CSM interaction.

2.5.2 Rise time limitations

A possible bias emerges when measuring rise times similar to or less than the survey cadence of 2–3 d. The discrete sampling of the light curve means rise times on these time-scales are typically less well constrained than longer rising events, where multiple observations sample the rising phase. With this in mind, we tested the predictive power of the GPR method by taking well-sampled light curves (with cadences $\sim$ 2 d or less between peak -50 and peak $+200$ d where the origin is the first alert detection) and resampled the light curves based on the sampling function of 20 events with much worse and more irregular cadences.[7] Using the actual light curve of the well-observed SN as the 'ground truth', we shift it according to the sampling

function of another light curve to emulate the 'ground truth' light curve being sampled differently.

Applying our standard rise time definition and constraints to these resampled light curves, we confirm that events maintain their classification as fast ($t_{25\_75} \leq 5$ d) or slow ($t_{25\_75} > 5$ d) risers regardless of sampling pattern. This was done to explore the range of a measured rise time based on the sampling function applied to a light curve. We find the range in rise times is increased for shorter rise times compared to longer risers, particularly at $t_{25\_75} \leq 5$ d – see Fig. A1. For t_{25_75} between 1–2 d, we see a range of ≈ 0.7 dex, for t_{25_75} between 3–5 d, we see a range of ≈ 0.4 dex, and for $t_{25\_75} > 5$ d, there is a range ≈ 0.2 dex.

Our t_{25_75} metric requires consideration for Type IIb SNe, which often show double-peaked light curves due to the shock cooling (SC) peak lasting hours to days, followed by a radioactively powered peak (Chevalier 1992; Richmond et al. 1994; Chevalier & Fransson 2008). As we are only concerned with measuring the rise time and peak magnitude for Type IIb and Type IIn and not progenitor properties, this remains an adequate descriptive measurement to characterize these SNe.

3 POPULATION PROPERTIES

In Fig. 5, we show the luminosity-duration phase-space distribution of all classified SNe (Type I and Type II) in the BTS sample (as of 2023 December 31). Fig. 5 is included to both show the increased number of events as compared to Perley et al. (2020) (Fig. 7a from

---

[6]WebPlotDigitizer: https://apps.automeris.io/wpd/.

[7]Chosen by finding events with an average cadence from peak -50 – peak $+ 200$ d ≥ 5 d.
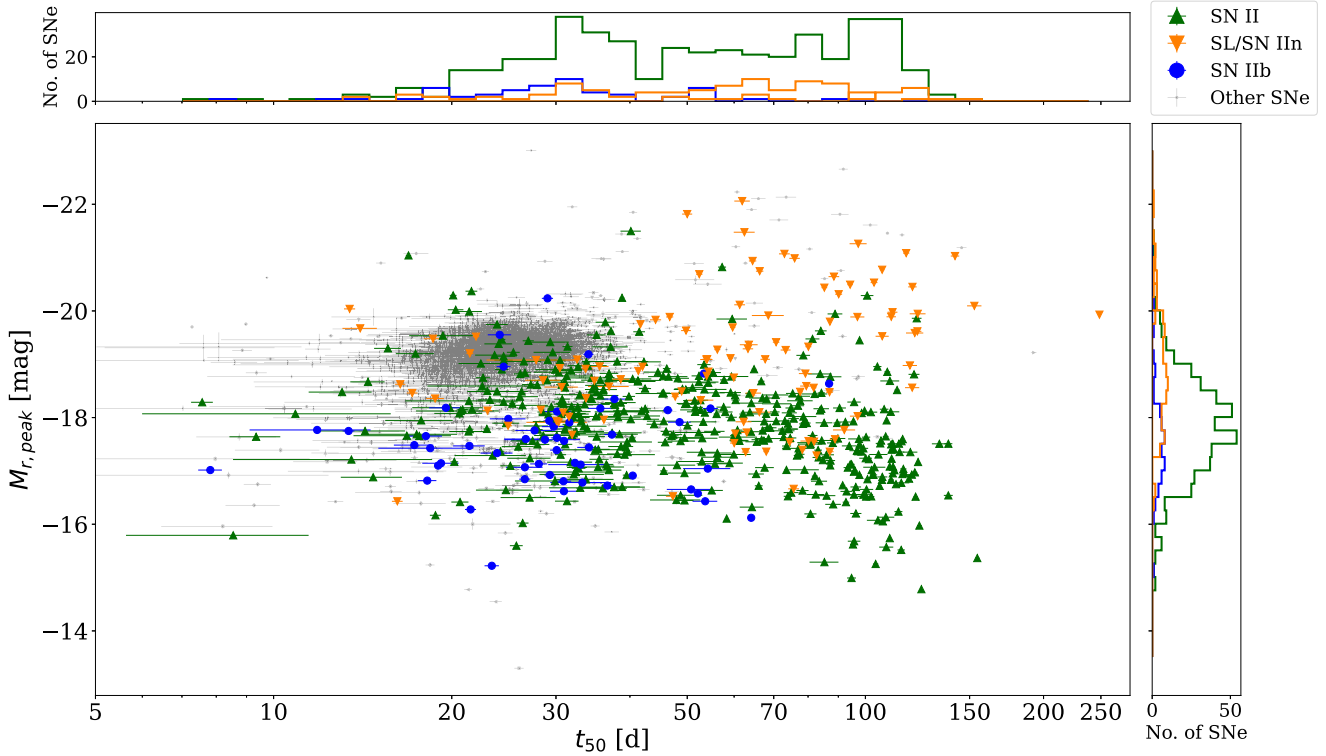
Figure 5. Phase-space diagram showing peak absolute magnitude in ZTF r ($M_{r,\mathrm{peak}}$) versus rest-frame duration above half-maximum brightness (t_{50}) for all SNe with $m_{\mathrm{peak}} \leq 19$ mag classified in the BTS through 2023 December 31. Type II SNe are colour-coded (large triangles and circles) by subtype, with other SN classes (e.g. Ia, Ib/c, SLSNe-I) shown in grey (small dots) for comparison. $M_{r,\mathrm{peak}}$ corrected for Galactic extinction only.

1D interpolation of data points).[8] and to demonstrate the reliability of GPR when measuring light-curve parameters due to the likeness between the two figures. Classifications and redshifts used in this work are part of the upcoming BTS classification paper (Qin et al., in preparation) for events with a $m_{\mathrm{peak}} \leq 18.5$ mag. For events with a $m_{\mathrm{peak}} > 18.5$ mag, we used the current TNS classifications stored on an internal BTS catalogue.[8] We do not expect the provisional nature of these classifications to significantly impact the study.

3.1 Overall distribution

Studies of the relationship between rise time and peak luminosity in Type II SNe have yielded conflicting results. Significant correlations have been reported for Type II, IIb, and IIn SNe (e.g. González-Gaitán et al. 2015; Pessi et al. 2019; Hiramatsu et al. 2024), suggesting the rise and peak may be intrinsically coupled by their power source. However, other analyses find no significant correlation (e.g. Gall et al. 2015; Rubin et al. 2016; Valenti et al. 2016; Nyholm et al. 2020). These discrepant findings likely stem from small sample numbers, limiting their statistical power to comment of population characteristics.

Motivated by the possibility of an enhanced population with fast rises and luminous peaks, either from SBO occurring in the CSM or at the surface of the star, we tested the strength of any existing correlation between t_{25_75} and $M_{g,\mathrm{peak}}$. For Type II SNe, a Spearman rank test between t_{25_75} in ZTF g and $M_{g,\mathrm{peak}}$ finds a correlation,

with a correlation coefficient $\rho = -0.21$ and p-value $p < 10^{-5}$. The scatter present in the correlation is likely caused by the large diversity of Type II SNe and lack of clear division within Type II SNe (e.g. IIP versus IIL versus 87A-like) as from Fig. 4, it can be seen that Type II SNe occupy both bright and faint, fast and slow regions, see Fig. 3.

In our sample of 110 Type IIn SNe (which includes 16 SNe classified as superluminous), we find $\rho = -0.18$ and p-value $p \sim 0.05$, a correlation both weaker and less significant than the recent findings of Hiramatsu et al. (2024). We see great diversity in our Type IIn light-curve morphology, which seems to suggest a range of progenitor pathways are possible, with a large range in t_{25_75} of $\sim$2 to 40 d and $M_{g,\mathrm{peak}}$ of -22.20 to -17.01 mag. As Type IIn SNe are well understood to be CSM-driven (e.g. Schlegel 1990; Fassia et al. 2000; Smartt 2009; Smith et al. 2010; Taddia et al. 2013; Ransome et al. 2021), and under this scenario it is expected that both the rise time and luminosity increase with the amount of CSM present (continuing the interaction), this possible correlation is not surprising (Section 6). For Type IIb SNe, we find no significant correlation as $p > 0.1$.

3.2 Volume-corrected distributions

With a highly complete magnitude-limited survey, we can perform a volume correction such that we can offer a more accurate representation of the true distribution of properties for a given population of SNe. The corrections account for intrinsic observational biases that favour the detection of more luminous events since they can be observed to greater distances in a magnitude-limited survey (Malquist bias; Malmquist 1920).

The volumetric correction we apply is according to a $1/V_{\mathrm{max}}$ weighting (Schmidt 1968). Initially, we perform a magnitude cut at

---

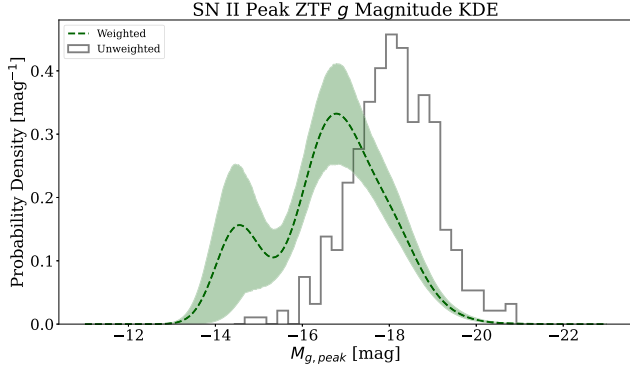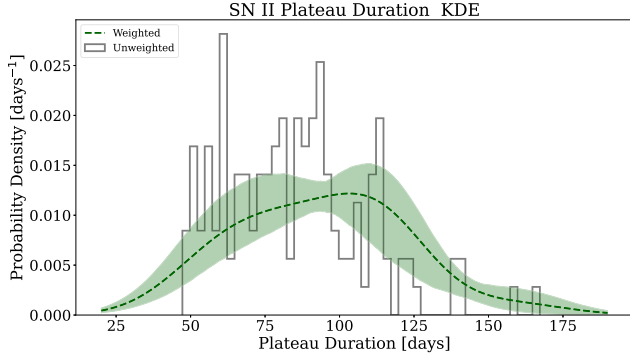[8]Also available to see on the BTS Homepage: https://sites.astro.caltech.edu/ztf/bts/bts.php.

(a) Type II $M_{g,peak}$ KDE distribution.

(b) Type II $t_{\rm plat}$ KDE distribution.

Figure 6. $M_{g,\rm peak}$ and $t_{\rm plat}$ KDE distribution for spectroscopically classified Type II SNe. We plot the weighted KDE distributions as the dashed line (darker colours) and the unweighted histogram in solid (black).

$m_{\rm peak} = 18.5$ mag given that the BTS is $\gtrsim 95$ per cent complete at this level. The peak magnitude cut reduces the sample to 377 Type II SNe, 81 Type IIn SNe, and 35 Type IIb SNe. $d_{l,\rm max}$ is calculated assuming a limiting magnitude of 18.5 mag, an average Galactic extinction, $A_{g,\rm Gal}$, of 0.19 mag (calculated using the $A_{g,\rm Gal}$ of the sample) and the ZTF g peak absolute magnitude of the GP model, $M_{g,\rm peak}$ — which is standardized to the rest-frame ZTF g band, corrected only for Milky Way extinction and not host extinction. We calculate $V_{\rm max}$ to be $d_{l,\rm max}^3/(1 + z)^3$ (based on the comoving distance), and use its reciprocal for weighting after normalizing the weights to unity.

To represent the intrinsic distribution of parameters, we use kernel density estimation (KDE). For each observed value, we generate a normalized Gaussian kernel centred on that real value and weight each Gaussian as $1/V_{\rm max}$. The width (sigma) of each kernel is optimized using cross-validation (e.g. Wu 1997). This approach estimates the underlying probability density function of the parameter distribution. We also normalize the KDE by the sum of weights, allowing us to account for Malmquist bias.

We quantify uncertainty in the weighted KDE as a 80 per cent CI, calculated by bootstrapping our sample with replacement. Similarly, we compute the ECDF with 95 per cent CI for unweighted distributions and bootstrapped 80 per cent confidence intervals for weighted distributions.

3.3 Data exploration

After weighting the distributions, we create weighted KDEs for direct light-curve properties of Type II SNe $M_{g,\rm peak}$, $t_{\rm plat}$, Figs 6(a) and (b), and t_{25_75} for all classes, Figs 7(a)–(c). We extract various statistical
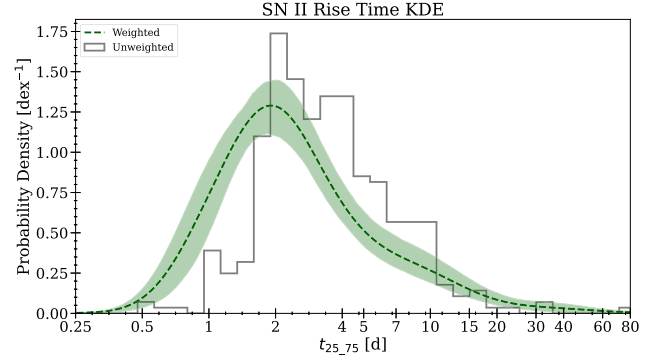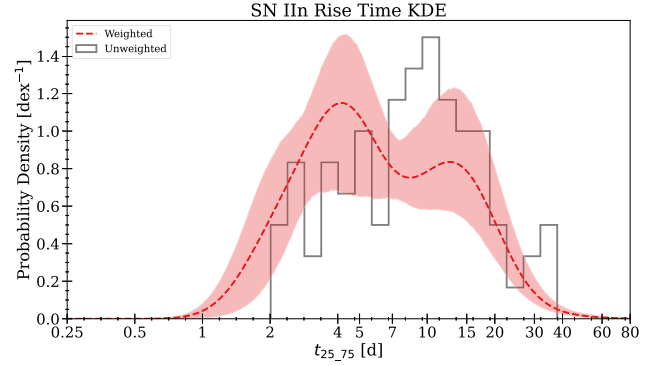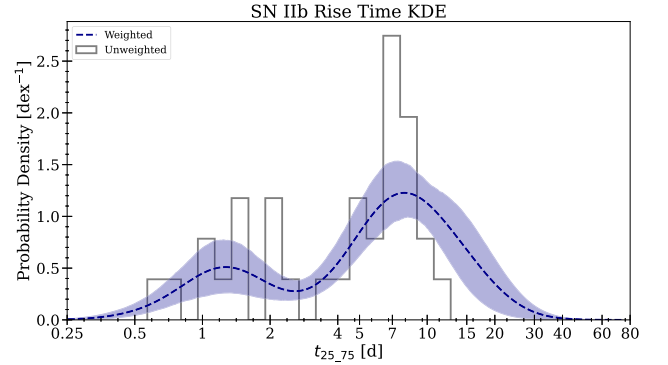

(a) Type II t_{25_75} KDE distribution.

(b) Type IIn t_{25_75} KDE distribution.

(c) Type IIb t_{25_75} KDE distribution.

Figure 7. t_{25_75} KDE distribution for spectroscopically classified Type II, Type IIn, and Type IIb with their associated 80 per cent CIs. We plot the weighted KDE distributions in the dashed lines (darker colours) and the unweighted histogram in solid (black).

properties relating to t_{25_75}, $M_{g,\rm peak}$, $(g - r)_{g,\rm max}$, and $t_{\rm plat}$ of each subclass from the KDE distributions and show these in Table 4, with uncertainties based on the 1σ standard deviations for each quantity.

Our demographic analysis of Type II SNe reveals a median absolute magnitude of $M_{g,\rm peak} = -16.71 \pm 0.25$ mag and a median rise time of $t_{25\_75} = 2.18^{+0.25}_{-0.23}$ d. From the volume-weighted ECDF, we find that 82^{+11}_{-12} per cent of the population has $M_{g,\rm peak} \leq -15$ mag, with the first and third quartiles at -16.03 and -17.44 mag, respectively. Most notably, 84 ± 3 per cent of the weighted population exhibits remarkably brief rise times (≤ 5 d), with first and third quartiles at 1.65 and 3.38 d. These distributions highlight the significant heterogeneity within the Type II SN population.
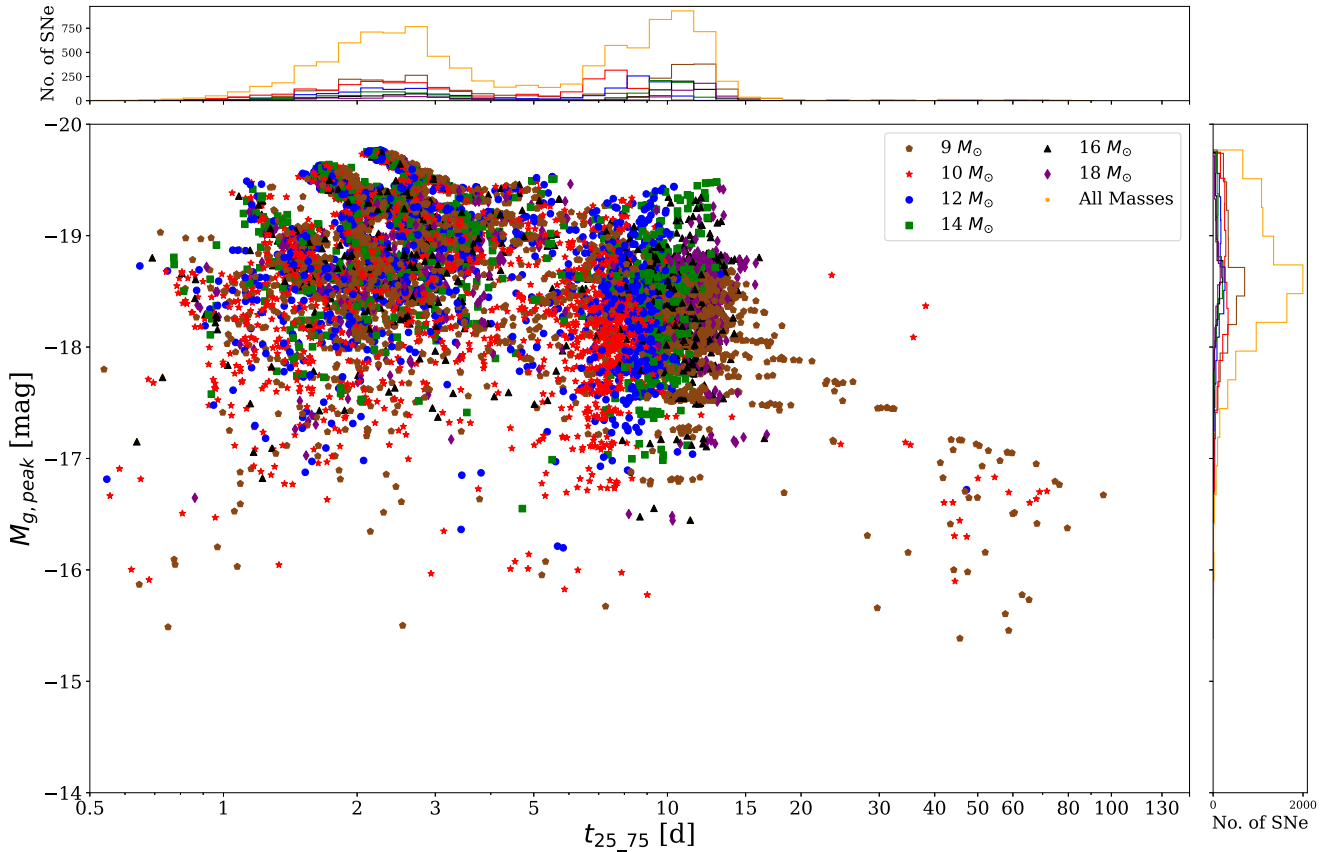
Figure 8. t_{25_75} versus $M_{g,\mathrm{peak}}$ distribution for the theoretical light-curve grid from M23, with points drawn from a sample of 10 000 models colour/shape-coded and by progenitor mass. Models are weighted by $V_{\mathrm{max}} \times M_{\mathrm{ZAMS}}^{-2.35}$, combining volume-limited sampling (calculated using a magnitude limit of 18.5 mag) with the Salpeter IMF. This weighting scheme reproduces both the observational bias against fainter events and the natural frequency of different progenitor masses.

4 METHODS II – COMPARISON TO SIMULATED LIGHT CURVES

Light-curve models are increasingly incorporating CSM or extended stellar envelopes (e.g. Hillier & Dessart 2012; Dessart, Audit & Hillier 2015; Das & Ray 2017; Dessart, Hillier & Audit 2017; Morozova et al. 2018; Tinyanont et al. 2022; Morag, Sapir & Waxman 2023; Moriya et al. 2023b; Pearson et al. 2023). Morozova et al. (2018) demonstrated that including CSM in SNEC[9] (Morozova et al. 2015) models significantly improved fits for 20 well-observed, multiband light curves to estimate progenitor parameters, such as R_{CSM}, CSM density, and M_{CSM} (see figs 2 and 3 and table 2 in Morozova et al. 2018). Similar conclusions emerge from studies by Das & Ray (2017), Bruch et al. (2023), Moriya et al. (2023b), Irani et al. (2024), and Jacobson-Galán et al. (2024a), which collectively find that substantial CSM masses near Type II SN progenitors are common and deposited shortly before core-collapse.

While fitting detailed physical models to the entire BTS Type II sample is possible, the computational demands and data heterogeneity make empirically derived relationships more practical for large-scale analysis. Our GP parameter catalogue enables efficient estimation of CSM properties through use of empirical relations. Additionally, we leverage this catalogue to investigate progenitor iron core masses ($M_{\mathrm{Fe,Core}}$), which significantly influence neutron star formation and properties (Barker et al. 2022; Barker, O'Connor &

Couch 2023). By applying simulation-based empirical relations to our light-curve parameters, we provide constraints on $M_{\mathrm{Fe,Core}}$ distributions (see Appendix A6).

4.1 Measuring theoretical light-curve metrics

To probe the physical origin of the rise time distribution shown in Fig. 4, we leverage our highly complete observational sample and the extensive grid of theoretical light curves from Moriya et al. (2023b, hereafter M23) using STELLA (Blinnikov et al. 1998, 2000, 2006). This comparison between observations and models enables us to systematically explore how progenitor and CSM properties shape the observed diversity. The models from M23 are some of the most comprehensive performed to date, as they sample several progenitor zero-age main-sequence masses, (M_{ZAMS}; 9–18 M$_\odot$), $\dot{M}$ (10^{-5}–10^{-1} M$_\odot$yr^{-1}), RSG wind structure parameter, (β[10]; 0.5–5), and R_{CSM} (10^{14}–10^{15} cm) among other progenitor properties (see table 2 in M23 for more details). The published grid contains over 200 000[11] models sampled from these parameters and is a base for comparing observed light curves.

To derive M_{CSM}, we first calculate the wind velocity, v_{wind}, at R_{CSM} using the velocity profile from Eq. 2 in Moriya et al. (2023b), which

---

[9]Supernova ExplosioN Code.

[10]Determined by the efficiency of wind acceleration, for RSGs $\beta > 1$ (Moriya et al. 2023b).

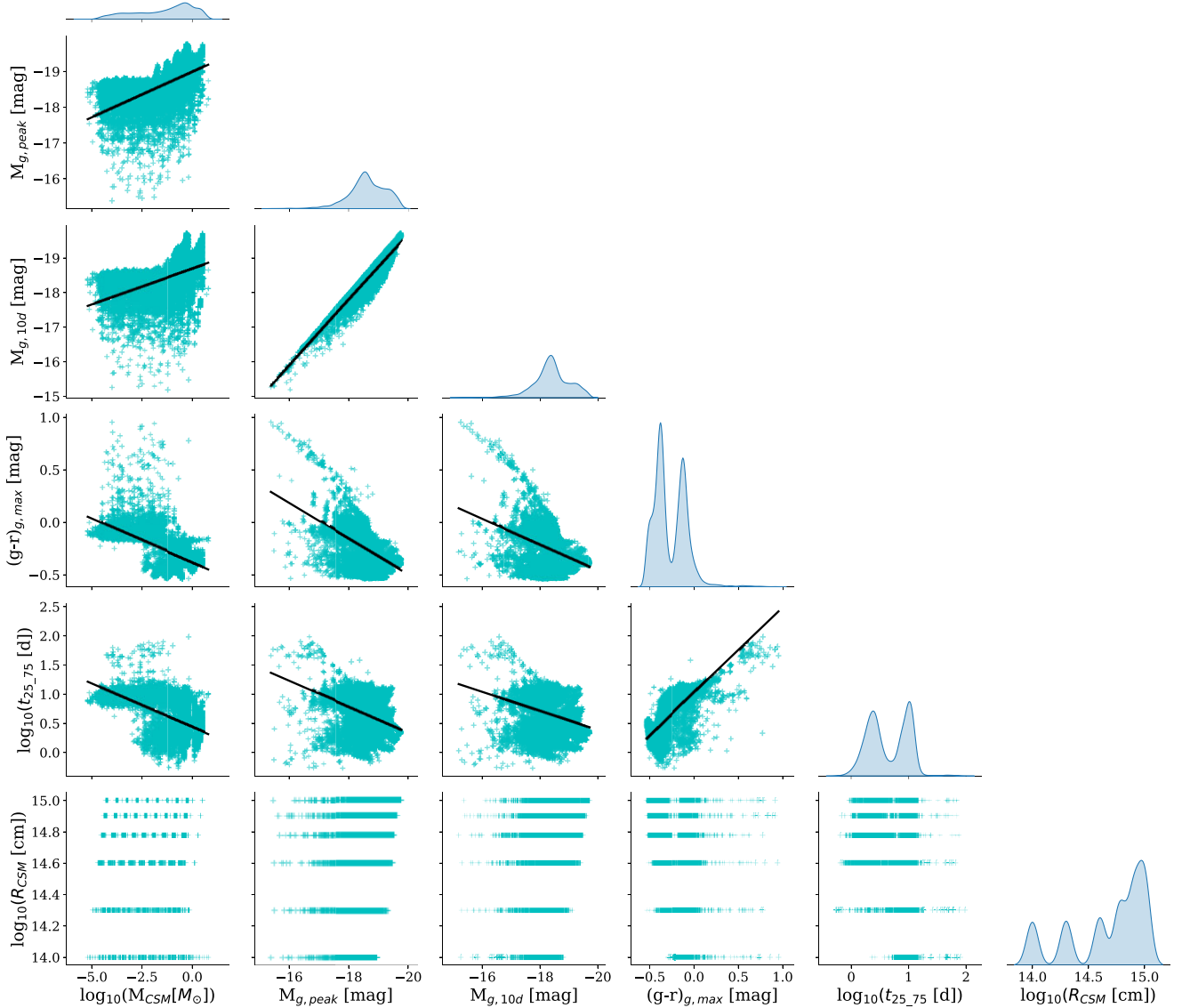[11]Published model grid can be found at Moriya 2023a.

Figure 9. Corner plot showing the relationship between M23 theoretical light-curve parameters measured in this work, t_{25_75}, $M_{g,\mathrm{peak}}$, $(g - r)_{g,\mathrm{max}}$, and $M_{g,10d}$ to the M_{CSM} and R_{CSM} values returned in the modelling. The solid black line is a first-order polynomial fit to the data.

depends on β and the progenitor radius $R_\odot$. M_{CSM} is calculated using $M_{\mathrm{CSM}} = \dot{M} \times R_{\mathrm{CSM}}/v_{\mathrm{wind}}$.

We measure various rise times – including the same t_{25_75} described in Section 2.5 – directly from the M23 ZTF bandpass light curves, in addition to absolute magnitudes (at peak and various N days after peak), magnitude decline rates and colours, e.g. $(g - r)_{g,\mathrm{max}}$ – Fig. 1 shows example measurements using ZTF SN light curves.

With the empirically measured light-curve parameters from M23, we create a similar luminosity-rise distribution plot[12] of t_{25_75} versus $M_{g,\mathrm{peak}}$ in ZTF g – see Fig. 4. We apply a probabilistic weighting of $V_{\mathrm{max}} \times M_{\mathrm{ZAMS}}^{-2.35}$ to the M23 models to mimic the combined effects of the initial mass function (IMF; Salpeter 1955) and Malmquist bias on an observed sample, and draw 10 000 events to show in Fig. 8

In Fig. 8, we see a clear bimodality, suggesting the dichotomy seen in observations is reflecting the transition between purely SC

dominated rises and rises dominated by the interaction heating from SBO shocking the CSM (e.g. Irani et al. 2024; Jacobson-Galán et al. 2024a). Correlation tests between progenitor-SN parameters confirm this dichotomy stems from significant relationships between CSM properties and light-curve observables, as well as between different CSM parameters.[13] This is further evidenced by the colour gradient seen when we apply a colour map based on $\dot{M}$ or R_{CSM} – see Appendix A5 for further details.

Two distinct populations emerge in the theoretical models: fast risers ($t_{25\_75} \leq 5$ d) with moderately more luminous peaks, possessing higher M_{CSM} and smaller R_{CSM} (e.g. confined and dense); and slower risers ($t_{25\_75} > 5$ d) with overall less luminous peaks, less massive M_{CSM} and larger R_{CSM} (e.g. less confined and less dense). Within the slower population, the most luminous events still require substantial M_{CSM}, suggesting CSM mass remains a key driver of peak luminosity.

---

[12]We also included unpublished 9 and 10 M$_\odot$ mass progenitor models with lower and higher explosion energies than in M23.

[13]Correlations between CSM parameters likely reflect physics pre-defined in the simulations.

Table 4. Mean and median of the volume corrected KDE for t_{25_75}, ZTF $M_{g,\text{peak}}$, $(g-r)_{g,\text{max}}$, and t_{plat} in the final sample, measured directly using the GPR described in Sections 2.3 and 2.3.1. Uncertainties reported here are the 1σ standard deviation on the bootstrapped values.

Type	Weighted				Unweighted			
	Mean	25th percentile	50th percentile	75th percentile	Mean	25th percentile	50th percentile	75th percentile
				t_{25_75} [d]				
II (377)	$2.48^{+0.30}_{-0.27}$	$1.65^{+0.57}_{-0.11}$	$2.18^{+0.25}_{-0.23}$	$3.38^{+0.31}_{-0.74}$	$3.39^{+0.12}_{-0.12}$	$2.13^{+0.07}_{-0.08}$	$3.21^{+0.11}_{-0.11}$	$5.09^{+0.47}_{-0.64}$
IIn (81)	$6.01^{+1.09}_{-0.92}$	$3.41^{+0.66}_{-0.94}$	$5.59^{+1.44}_{-1.14}$	$11.83^{+2.10}_{-1.71}$	$8.54^{+0.73}_{-0.67}$	$4.85^{+1.35}_{-1.48}$	$8.73^{+0.86}_{-0.78}$	$14.32^{+3.06}_{-2.22}$
IIb (35)	$4.97^{+1.27}_{-1.01}$	$2.00^{+0.61}_{-2.68}$	$6.32^{+1.72}_{-1.35}$	$8.59^{+0.67}_{-1.69}$	$3.99^{+0.61}_{-0.53}$	$1.79^{+0.69}_{-1.53}$	$4.87^{+0.93}_{-0.78}$	$7.54^{+0.89}_{-1.03}$
				$M_{g,\text{peak}}$ [mag]				
II (377)	-16.59 ± 0.29	$-16.03^{+0.28}_{-0.39}$	-16.71 ± 0.25	$-17.44^{+0.22}_{-0.09}$	-18.10 ± 0.05	$-17.54^{+0.10}_{-0.15}$	-18.11 ± 0.05	$-18.74^{+0.16}_{-0.08}$
IIn (81)	-18.19 ± 0.19	$-17.68^{+0.14}_{-0.12}$	-18.02 ± 0.21	$-18.82^{+0.56}_{-0.43}$	-19.35 ± 0.13	$-18.49^{+0.56}_{-0.43}$	-19.32 ± 0.13	$-19.98^{+0.55}_{-0.27}$
IIb (35)	-17.79 ± 0.17	$-17.45^{+0.12}_{-0.16}$	-17.79 ± 0.19	$-18.37^{+0.35}_{-0.24}$	-18.15 ± 0.14	$-17.58^{+0.31}_{-0.27}$	-18.09 ± 0.14	$-18.76^{+0.46}_{-0.40}$
				$(g-r)_{g,\text{max}}$ [mag]				
II (377)	0.17 ± 0.05	$0.01^{+0.01}_{-0.02}$	0.09 ± 0.03	$0.25^{+0.09}_{-0.14}$	0.04 ± 0.01	$-0.04^{+0.02}_{-0.03}$	0.02 ± 0.01	$0.08^{+0.02}_{-0.03}$
IIn (81)	0.21 ± 0.08	$0.00^{+0.01}_{-0.02}$	0.10 ± 0.07	$0.49^{+0.32}_{-0.02}$	0.11 ± 0.02	$-0.01^{+0.01}_{-0.02}$	0.08 ± 0.01	$0.16^{+0.06}_{-0.05}$
IIb (35)	0.25 ± 0.06	$0.00^{+0.02}_{-0.04}$	0.26 ± 0.06	$0.41^{+0.04}_{-0.04}$	0.13 ± 0.04	$-0.03^{+0.11}_{-0.04}$	0.12 ± 0.04	$0.31^{+0.16}_{-0.07}$
				t_{plat} [d]				
II (151)	93.86 ± 6.39	$71.89^{+10.63}_{-6.87}$	93.88 ± 7.96	$112.50^{+14.85}_{-1.25}$	83.98 ± 2.11	$61.25^{+2.51}_{-5.47}$	82.29 ± 2.19	$96.45^{+4.75}_{-9.81}$

This bimodality emerges naturally from the underlying physics rather than parameter choices, hinting at fundamental differences in mass-loss mechanisms.

For slower rising events, the correlation between t_{25_75} and CSM parameters lessens, giving way to a stronger dependence on progenitor mass (M_{ZAMS}), which serves as a proxy for progenitor radius. This transition reflects both the increasing dominance of light traveltime and diffusion processes in more massive, extended progenitors, as well as the slower cooling of the shocked envelope (e.g. Nakar & Sari 2010; Ofek et al. 2010; Tominaga et al. 2011; Morozova et al. 2016; Irani et al. 2024). Notably, for events with longer rise times (≥ 5 d), the progenitor radius influences rise time by affecting the SBO time and location (Chevalier & Irwin 2011; Moriya et al. 2011; Svirski, Nakar & Sari 2012; González-Gaitán et al. 2015; Morozova et al. 2016), though the light-curve evolution is still predominantly shaped by CSM interaction rather than envelope cooling, depending critically on the CSM density profile (Moriya et al. 2023b; Irani et al. 2024).

Notably, the contrast between the smooth distribution in our observational data (Fig. 4) and the distinct bimodality in theoretical models (Fig. 8) implies that there are physical process that lead to restrictive prior distributions on progenitor properties, deviating notably from the exploratory, uniform parameter sampling employed in M23 for physical progenitor parameters.

5 PHYSICAL PROGENITOR PROPERTY INFERENCE ANALYSIS

To quantify the percentage of RSGs that are surrounded by significant components of CSM at the time of core-collapse, we use the early light curve to infer the presence and properties of CSM. As the rise of Type II SNe is highly sensitive to the CSM parameters and progenitor radius (e.g. Morozova et al. 2016, 2018; Tinyanont et al. 2022; Moriya et al. 2023b; Pearson et al. 2023; Irani et al. 2024), we can estimate and place constraints on these properties from photometry alone. The high cadence and good coverage on the rise specifically, combined with the high completeness of the BTS lends itself well to such a detailed study.

5.1 Defining light curve–CSM relations

We examined relationships between observational and progenitor parameters by performing systematic correlation tests across the M23 model grid. Fig. 9 reveals significant pairwise correlations between progenitor properties (e.g. M_{CSM} and R_{CSM}) and the observational parameters measured in this work ($M_{g,\text{peak}}$ and t_{25_75}), providing a statistical foundation for our subsequent parameter estimation.

When we analyse simple two-variable analysis, e.g. $M_{\text{CSM}} = f\left(M_{g,peak}, t_{25\_75}\right)$, the relations show substantial scatter, indicating that these parameters alone cannot capture the complex CSM–ejecta interaction physics. To better characterize the evolution, we decompose the rise time into: 20–60 per cent, t_{20_60}, and 60–90 per cent, t_{60_90}, or 20–50 per cent, t_{20_50}, and 50–80 per cent, t_{50_80}. This approach provides additional diagnostics through the shape of the rise. Additionally, we include ZTF $g-r$ colour at ZTF g peak flux, $(g-r)_{g,\text{max}}$, and the ZTF g absolute magnitude at 10 d post-ZTF g peak, $M_{g,10d}$, to account for any contribution to the early plateau or post-peak behaviour by the CSM (or lack of). We perform multiple regression analysis, attempting to express M_{CSM} empirically as $M_{\text{CSM}} = f\left(M_{g,\text{peak}}, t_{20\_60}, t_{60\_90}, (g-r)_{g,\text{max}}, M_{g,10d}\right)$ and a similar expression for R_{CSM}.

We analyse the relationship between CSM parameters and observables using multivariate polynomial regression, implemented via the `statsmodels ols` package in PYTHON. For M_{CSM}, we achieve $R^2 > 0.5$ across most polynomial orders, indicating robust correlations. The relationships with R_{CSM} exhibit somewhat weaker but still significant correlations, as detailed in Table 5. Our goal is to develop reliable predictive relationships that enable rapid estimation of physical parameters (M_{CSM} and R_{CSM}) from observable quantities such as t_{25_75} and $M_{g,\text{peak}}$.

The performance of each polynomial order is analysed using the Bayesian information criterion (BIC; Table 5). We split the correlation testing into $t_{25\_75} \leq 5$ and > 5 d as the correlation appears strongest for the fast-rising models $t_{25\_75} \leq 5$ d and underpredicts M_{CSM} for several long-rising $t_{25\_75} > 5$ d models by up to 1–2 orders of magnitude – see Fig. 10. This likely reflects the physics of CSM interaction: confined, dense CSM shells enable a rapid and efficient conversion of kinetic energy to radiation, producing brief, bright

Table 5. Comparing the performance over different orders of polynomials used in the multiple regression to determine the relations between observed features and CSM properties, $M_{\rm CSM}$ and $R_{\rm CSM}$, using models from M23.

| Data regime	Formula	Order	D.o.F	R^2	$M_{\rm CSM}$ BIC	RMS [dex]	R^2	$R_{\rm CSM}$ BIC	RMS [dex]
All	Equation (A2)	1	298980	0.47	839 466	0.30	0.14	175 163	0.12
All	Equation (A3)	2	298970	0.57	777 999	0.28	0.23	141 781	0.12
All	Equation (A4)	3	298950	0.62	736 557	0.26	0.28	121 588	0.11
≤ 5 d	Equation (A2)	1	112263	0.45	210 328	0.21	0.47	−89 654	0.07
≤ 5 d	Equation (A3)	2	112253	0.52	193 260	0.20	0.53	−103 416	0.06
≤ 5 d	Equation (A4)	3	112233	0.58	180 362	0.19	0.55	−109 371	0.06
> 5 d	Equation (A2)	1	186711	0.29	536 827	0.31	0.04	146 335	0.13
> 5 d	Equation (A3)	2	186701	0.41	502 875	0.29	0.07	138 972	0.13
> 5 d	Equation (A4)	3	186681	0.48	480 037	0.27	0.12	129 340	0.13
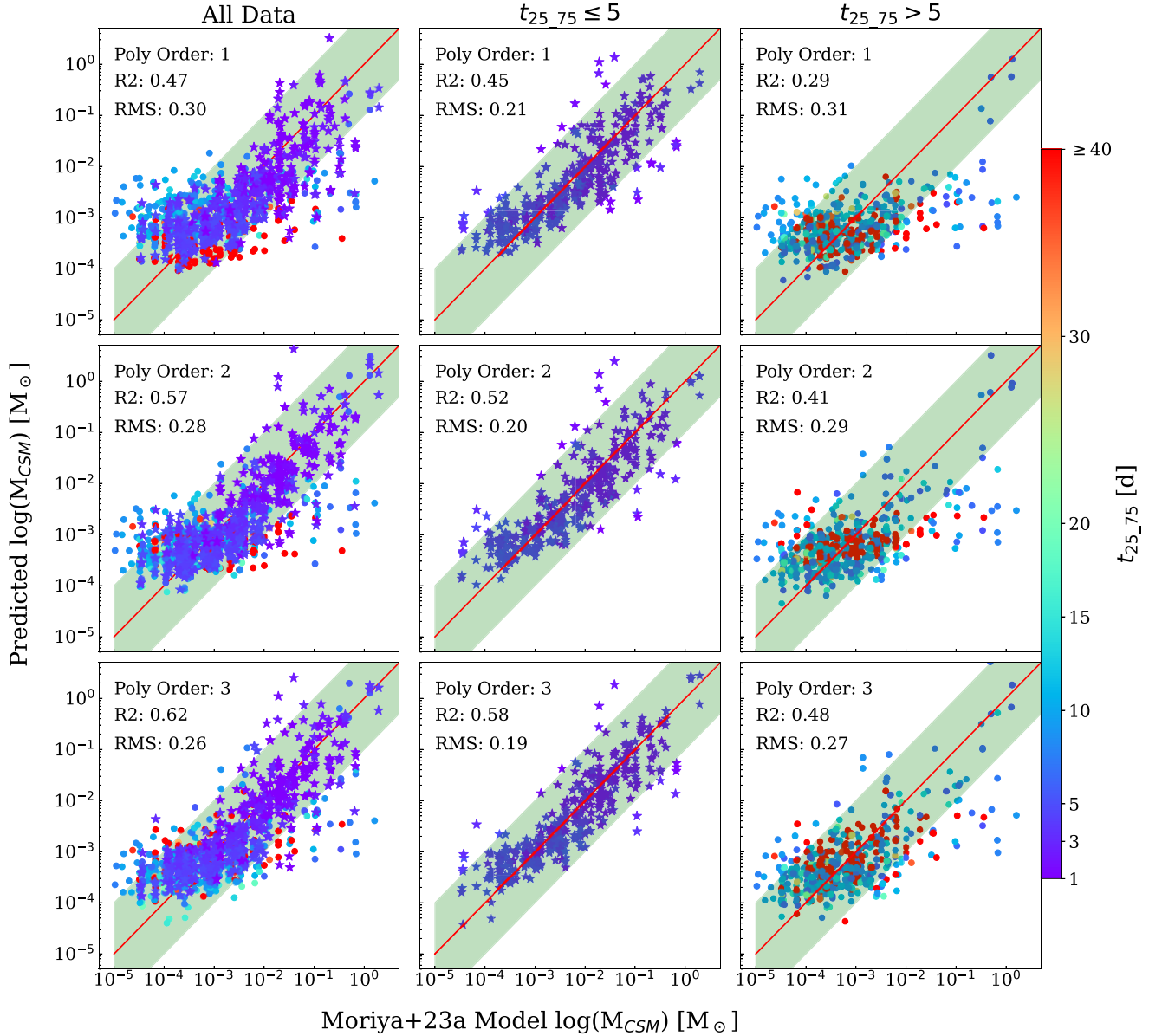
Figure 10. Multivariate analysis results of the predicted $M_{\rm CSM}$ mass (y-axis) versus the M23 $M_{\rm CSM}$ mass (x-axis). The top, middle, and bottom rows are polynomial orders 1, 2, and 3, respectively. The first column contains all the data and stars are those with $t_{25\_75} \le 5$ d with the second and third rows containing only data with $t_{25\_75} \le 5$ d and $t_{25\_75} > 5$ d to show how the correlations predictive power decreases significantly with $t_{25\_75} \ge 5$ d. The diagonal red line is the 1:1 line with the green shaded region showing 1 order of magnitude above and below. 1000 models were used in the plot to avoid overcrowding.

emission with fast rise times (e.g. Moriya et al. 2011; Chevalier 2012; Tinyanont et al. 2022; Pearson et al. 2023; Li et al. 2024). In contrast, longer rise times can result from either more extended CSM configurations where energy is released more gradually, or from different physical processes entirely, weakening the direct correlation between M_{CSM} and light-curve properties (e.g. Moriya 2023; Jacobson-Galán et al. 2024a).

The systematic underprediction of M_{CSM} for models with higher masses and longer rise times motivated our inclusion of post-peak magnitude as an additional predictor variable. For R_{CSM}, the strongest correlations are consistently found in the subset of models with $t_{25\_75} \leq 5$ d.

We restrict polynomial orders to three or less to avoid introducing unphysical complexity into the model. For M_{CSM}, the reduction in residuals and increasing R^2 from first to third order indicates improved model performance, with third-order polynomials providing the best balance between model complexity and fit quality across both data regimes ($t_{25\_75} \leq 5$ and > 5 d), highlighting the importance of curvature terms in the relation. To better visualize the scatter in these correlations, we add 10 per cent random scatter to the plotted R_{CSM} values in Fig. A6.

R_{CSM} measurements become most reliable in regimes where M_{CSM} is large enough to influence observables such as $M_{g,peak}$ and t_{25_75} significantly (e.g. make $M_{g,peak}$ brighter or t_{25_75} shorter). We determine the critical value – below which the CSM does not notably influence the early light curve – of M_{CSM} by varying the physical parameters $\dot{M}$, R_{CSM}, and β independently (noting that M_{CSM} is a function of these three variables within the model). Below this minimum M_{CSM}, the CSM will become too diffuse to meaningfully influence the early light-curve evolution, effectively transitioning to a regime where CSM interaction is negligible. This physical expectation is reinforced by the distinct bimodality observed in M23's theoretical models,

Fig. 8, which reveals these two distinct populations: one where CSM properties strongly correlate with observables ($M_{g,peak}$ and t_{25_75}); and another showing no clear correlation, indicating negligible CSM influence. Our analysis reveals an observational transition at $M_{CSM} \approx 10^{-2.5}$ M$_\odot$, below which we cannot detect significant changes in observed parameters ($M_{g,peak}$ and t_{25_75}) – see Appendix A9 and Fig. A7 for more details. Given this limitation, we restrict our subsequent analysis of R_{CSM} and $\dot{M}$ to events where the predicted M_{CSM} exceeds this threshold.

When we re-analysed the R_{CSM} correlations with this M_{CSM} threshold ($\geq 10^{-2.5}$ M$_\odot$), we find substantially stronger correlations, especially for rapid-rise events ($t_{25\_75} \leq 5$ d). For these rapid-rise events, our third-order polynomial fit achieves $R^2 = 0.59$ with an RMS scatter of 0.06 dex. Slower rising events ($t_{25\_75} > 5$ d) still show a weaker correlation with $R^2 = 0.38$ and larger scatter (RMS = 0.10 dex). Based on these results, we adopt the third-order polynomial fits for R_{CSM} in both time regimes. See Table A3 for the final coefficients.

5.2 Mass-loss rate

The conversion of M_{CSM} estimates to $\dot{M}$, equation (2), requires the stellar wind velocity (v_{wind}). Although M23's models are parametrized using $\dot{M}$ (which implicitly assumes a wind velocity), the resulting light curves depend solely on the CSM density profile at the time of explosion. Consequently, our M_{CSM} measurements can be directly compared to their models, with the assumed wind velocity affecting only the conversion between M_{CSM} and $\dot{M}$, not the

underlying physics.

$$\frac{\dot{M}}{M_\odot \ yr^{-1}} = \left(\frac{M_{CSM}}{M_\odot}\right)\left(\frac{v_{wind}}{10 \ km \ s^{-1}}\right)\left(\frac{R_{CSM}}{10^{14} \ cm}\right)^{-1}. \qquad (2)$$

For Type II SNe, we assume a stellar wind velocity of 10 km s^{-1}, consistent with previous literature (e.g. Davies et al. 2022; Moriya et al. 2023b). We also calculate the time in which the mass was removed $t_{removal} \sim R_{CSM}/v_{wind}$. While M23 explored R_{CSM} from 10^{14}–10^{15} cm, we cannot uniquely determine $\dot{M}$ from our observations alone. For comparison with previous studies, we adopt a fiducial value of $R_{CSM} = 5 \times 10^{14}$ cm.

5.3 Progenitor property volume-corrected distributions

After weighting the distributions, we create weighted KDEs for empirically derived progenitor properties M_{CSM}, $\dot{M}$, and R_{CSM} – see Figs 11(a)–(c), respectively.

For comparison, recent studies of SN 2023ixf (e.g. Bostroem et al. 2023; Hiramatsu et al. 2023; Hosseinzadeh et al. 2023; Jacobson-Galán et al. 2023; Jencson et al. 2023; Li et al. 2024; Zimmerman et al. 2024) and SN 2024ggi (e.g. Chen et al. 2024, 2025; Shrestha et al. 2024; Jacobson-Galán et al. 2024b) prefer $\dot{M}$ between 10^{-3}–10^{-2} M$_\odot$yr^{-1} calculated by photometric and/or spectroscopic modelling of the event and its environment. For SN 2023ixf, we find $M_{CSM} \sim$ 0.1 M$_\odot$, $R_{CSM} \sim 6 \times 10^{14}$ cm, and $\dot{M} \sim 1 \times 10^{-2}$ M$_\odot$yr^{-1} respectively. Singh et al. (2024) and Moriya & Singh (2024) conduct a similar exercise, finding the best fitting M23 models to SN 2023ixf, and measure similar values for $\dot{M}$, 10^{-3}–10^{-2} M$_\odot$yr^{-1}, and $R_{CSM} \sim 5$–10×10^{14} cm. For SN 2024ggi, we find $M_{CSM} \sim 5 \times 10^{-3}$ M$_\odot$, $R_{CSM} \sim 3 \times 10^{14}$ cm, and $\dot{M} \sim 2 \times 10^{-4}$ M$_\odot$yr^{-1}, respectively.

We report the key statistics for measured M_{CSM}, $\dot{M}$, and R_{CSM} in Table 6 derived from their weighted respective KDEs. For the uncertainties on M_{CSM} and R_{CSM} quoted either in Table 6 or later, we use equation (A4) for M_{CSM} and R_{CSM} and resample each parameter 1000 times within their uncertainties using a uniform distribution – bounds set to be, for example, $[M_{g,peak} - \sigma_{M_{g,peak}}, M_{g,peak} + \sigma_{M_{g,peak}}]$. We then find the 1σ standard deviation. This method is repeated for $\dot{M}$ using equation (2).

Figs 12(a)–(c) are the ECDFs for M_{CSM}, $\dot{M}$, and R_{CSM} which show the empirical distribution of parameters for the weighted and unweighted samples. For the weighted ECDFs, we show the 80 per cent CI via the same bootstrapping method as previously described. For the unweighted ECDF, we perform a similar bootstrap with replacement to select from the sample and find the 95 per cent CI empirically following a similar routine of finding the difference 2.5th and 97.5th percentiles.

6 DISCUSSION

6.1 Luminosity and rise distributions

The volume-corrected sample of 377 Type II SNe yields a mean peak absolute magnitude in rest-frame ZTF g band of $M_{g,peak} = -16.59 \pm 0.29$ mag, with a median of $M_{g,peak} = -16.71 \pm 0.25$ mag. To place these results in context of previous studies, we compile peak luminosities from recent surveys in Table 7. While direct comparison is limited by filter differences – earlier surveys typically used $UBVRI$ rather than Sloan or ZTF filters – our mean and median weighted measurements in ZTF g can be broadly compared with Johnson–Cousins B- and V-band values, and show agreement within 1.5σ across all studies.

(a) M_{CSM} KDE Distribution.

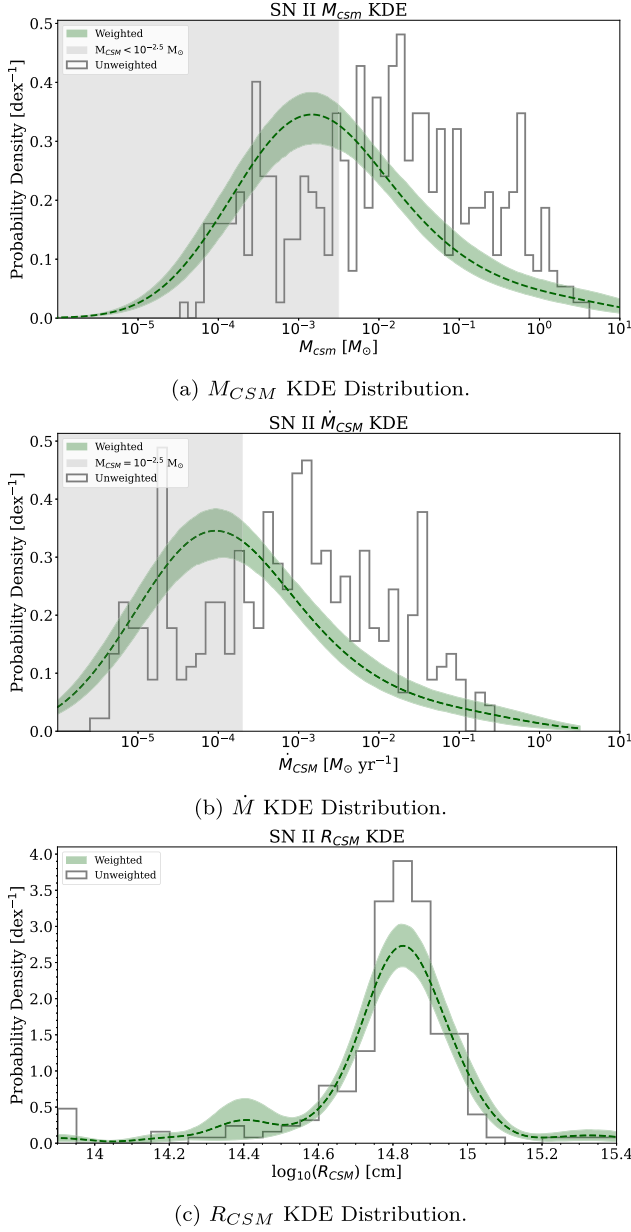(b) $\dot{M}$ KDE Distribution.

(c) R_{CSM} KDE Distribution.

Figure 11. Type II KDE for M_{CSM}, $\dot{M}$, and R_{CSM} along with their associated 80 per cent CI. The weighted distributions are the dashed lines (darker green) and the unweighted normalized histograms are solid (black). The shaded region on the KDE for M_{CSM} and $\dot{M}$ show the region below $10^{-2.5}$ M$_\odot$ (or corresponding to) where we find CSM does not impact observables.

When comparing our volume corrected mean $M_{g,\mathrm{peak}}$ to the entire M23 model grid (no weighting applied), we find the theoretical predictions are systematically brighter: mean $M_{g,\mathrm{peak}} = -17.88$ mag and median $M_{g,\mathrm{peak}} = -18.11$ mag. This luminosity difference reflects the the ability of our volume-complete sample to naturally capture the full diversity of Type II SNe, with the M23 grid focusing on systematically exploring parameter space rather than matching the observed luminosity distribution or the IMF.

We compared our sample with that of Das et al. (2025), which uses the ZTF Census of the Local Universe survey (CLU; De et al. 2020), and we are consist in the key overlapping measurement between the studies, with the luminosity distributions, Fig. 6(a), being in strong agreement.

We have limited overlap with Pessi et al. (2025), studying Type II SLSNe from ZTF, though we find 23^{+9}_{-7} per cent Type IIn SNe in our weighted sample have $M_{g,\mathrm{peak}}$ brighter than -19 mag – this is the most appropriate as we grouped Type IIn and SLSNe together – with a large range in $M_{g,\mathrm{peak}}$ -17.01 to -22.20 mag. Our unweighted median $M_{g,\mathrm{peak}}$ for Type IIn, -19.32 ± 0.13 mag, agrees with median values in Hiramatsu et al. (2024).

The observed correlation between $M_{g,\mathrm{peak}}$ and t_{25_75} for Type II SNe (excluding Types IIn and IIb) revealed in Section 3.1 is likely to be driven by a deficit of slow-rising, low-luminosity events. This weak correlation, also noted by Valenti et al. (2016), presents an intriguing discrepancy with theoretical predictions. While the M23 models (Fig. 8) predict this region of parameter space to be populated by explosions from low-mass progenitors, our BTS sample shows noticeably fewer such events than theoretically expected. Although we do detect some low-luminosity SNe with extended rise times ($t_{25\_75} \gtrsim 15$ d), their relative scarcity compared to model predictions is significant. Section 6.2 quantifies this population's occurrence rate relative to the broader Type II population.

Type II SNe exhibit diverse rise times, with their distribution (Fig. 4) suggesting a continuous rather than bimodal range of progenitor properties. The lack of bimodality in the observed t_{25_75} distributions is significant and likely reflects an overabundance of these events compared to their representation in the M23 grid. This continuous distribution is seen before and after the volume correction, Fig. 7(a), suggesting this is not a result of lacking observations of a particular population. The prevalence of events with both rapid rise times and high luminosities provides compelling evidence for dense CSM being common among Type II SNe. These characteristics are consistent with SBO within CSM (e.g. Moriya et al. 2011, 2018; Chevalier 2012; Das & Ray 2017; Tinyanont et al. 2022; Pearson et al. 2023; Li et al. 2024), as models without significant CSM struggle to simultaneously produce such fast rise times and enhanced peak brightness.

To investigate whether our results depend on the extinction correction, we also examined the distributions of all parameters if no extinction correction was applied. $M_{g,\mathrm{peak}}$, t_{25_75} and CSM parameters estimates changed by no more than 1σ. Since the host extinction correction affects only a small fraction of our sample, our conclusions about the physical parameter distributions remain largely unaffected. The $1/V_{\mathrm{max}}$ correction we apply to our observational sample addresses potential observational bias, but significant uncertainties remain in the faint end of the luminosity function – explored in detail by Das et al. (2025).

6.2 Long rising Type II SNe

Of note in Fig. 4 are the events with long rise times, $t_{25\_75} \gtrsim 25$ d. These events are slowly evolving, seemingly in the gap between Type IIn and the region of space the long simulated Type II light curves from Moriya (2023) occupy. There are five events in our sample with rise times ≥ 25 d that all have non-standard Type II light curves. Some of these SNe show resemblance to SN 1987A where the rise to peak is a slow hump or they have an early peak fainter than the main peak – see ZTF18acbwaxk/SN 2018hna in Fig. 3 for an example. To confirm the absence of narrow lines, and rule out misclassification of Type IIn SNe, we checked the classifying spectra and confirmed there were no narrow lines present in their spectral series – most have multiple high-resolution spectra.

When comparing the magnitude-limited BTS sample with the volume-limited ZTF CLU, only one event overlaps with the Sit et al. (2023) study – ZTF18acbwaxk/SN 2018hna ($t_{25\_75} \sim 35$ d,

Table 6. Mean and median of the volume corrected KDE for $M_{\rm CSM}$, $\dot{M}$, and $R_{\rm CSM}$ in the final sample. $M_{\rm CSM}$, $\dot{M}$, and $R_{\rm CSM}$ were inferred via linear relations involving GPR parameters. For $R_{\rm CSM}$, we exclude data where the corresponding $M_{\rm CSM} < 10^{-2.5}$ M$_\odot$ as we consider $M_{\rm CSM}$ lower than this to have a negligible effect on the observable parameters and cannot constrain $R_{\rm CSM}$ for lower $M_{\rm CSM}$. Values for $\dot{M}$ use a fiducial value of 5×10^{14} cm for $R_{\rm CSM}$. Uncertainties reported here are the standard deviation on the bootstrapped values. The mean, 25th percentile and median values for $M_{\rm CSM}$ are not reported here as they are below $10^{-2.5}$ M$_\odot$ and we cannot confidently constrain below this threshold. For the same reason, we do not report the mean, 25th percentile or median for $\dot{M}$ as this is below the $\dot{M}$ corresponding to $M_{\rm CSM} = 10^{-2.5}$ M$_\odot$.

Parameter	Units	Mean	25th percentile	50th percentile	75th percentile	Range	No.
				Weighted			
$M_{\rm CSM}$	$\times 10^{-3}$ M$_\odot$	–	–	–	$9.55^{+3.48}_{-5.79}$	$[0.11, 1.05 \times 10^3]^1$	377
$\dot{M}$	$\times 10^{-4}$ M$_\odot$yr^{-1}	–	–	–	$6.03^{+2.20}_{-3.61}$	$[3.22, 8.16 \times 10^2]^1$	377
$R_{\rm CSM}$	10^{14} cm	6.69 ± 0.92	$5.58^{+0.28}_{-0.28}$	6.56 ± 0.25	$7.84^{+0.19}_{-0.11}$	$[1.98, 14.11]$	253
				Unweighted			
$M_{\rm CSM}$	$\times 10^{-3}$ M$_\odot$	$10.61^{+1.79}_{-1.54}$	$1.34^{+1.91}_{-2.05}$	$11.62^{+2.05}_{-1.74}$	$93.87^{+36.22}_{-45.90}$	–	–
$\dot{M}$	$\times 10^{-4}$ M$_\odot$yr^{-1}	$6.70^{+1.15}_{-0.98}$	$0.85^{+0.41}_{-0.49}$	$7.54^{+1.40}_{-1.18}$	$59.25^{+25.22}_{-30.85}$	–	–
$R_{\rm CSM}$	10^{14} cm	6.55 ± 0.44	$5.72^{+0.51}_{-0.18}$	6.63 ± 0.12	$7.90^{+0.33}_{-0.31}$	–	–

Note. [1] The ranges reported are the 5th and 95th percentiles to remove outliers beyond the limits of the original data set.

$M_{g,\rm peak} \sim -15.99$ mag uncorrected). This limited overlap stems from different selection criteria: BTS captures brighter events (peak magnitudes < 18.5 mag), while CLU focuses on lower luminosity events in nearby galaxies. For Type II SNe with rise times > 25 d, we compute a rate relative to the CCSN rate found in Perley et al. (2020).

Before applying a magnitude cut for completeness, we identify 5/481 Type II SNe with $t_{25-75} \geq 25$ d from our sample. Accounting for observational bias, we find these long-rising events constitute $2.16^{+1.93}_{-0.60}$ per cent of the Type II SN population, with a weighted mean $M_{g,\rm peak} = -16.33$ mag, compared to -16.59 mag for the overall sample. After implementing an 18.5 mag completeness cut, we retain four long-rising events in our sample of 377 SNe, corresponding to a bias-corrected fraction of $1.43^{+1.28}_{-0.15}$ per cent with no significant change in $M_{g,\rm peak}$. These low rates, though limited by small statistics, confirm these events are rare and align with previous findings: Sit et al. (2023) report that SNe with $t_{25-75} > 40$ d comprise 1.4 ± 0.3 per cent of all CCSNe, while earlier studies found rates of 1.5–3 per cent (Smartt 2009; Kleiser et al. 2011; Pastorello et al. 2012).

6.3 CSM mass and radial extent

Our Type II SN sample reveals widespread evidence for substantial CSM present at the time of explosion. Accounting for observational biases through a volumetric weighting, 36^{+5}_{-7} per cent of events have $M_{\rm CSM} \geq 10^{-2.5}$ M$_\odot$, with the 80th percentile of the full sample being $1.56^{+1.12}_{-0.54} \times 10^{-2}$ M$_\odot$. In the unweighted sample, 67 ± 6 per cent of events show significant $M_{\rm CSM}$ ($\geq 10^{-2.5}$ M$_\odot$). These $M_{\rm CSM}$ estimates, and the corresponding $R_{\rm CSM}$, remain consistent when analysed without host-extinction corrections.

For events with massive CSM shells ($M_{\rm CSM} \geq 10^{-2.5}$ M$_\odot$), our weighted sample shows a median $R_{\rm CSM}$ of $\sim 6 \times 10^{14}$ cm, with nearly all events having inferred radii $\leq 10^{15}$ cm and a well-defined peak around this median (Figs 11c and 12c). The upper limit of $R_{\rm CSM} \leq 10^{15}$ cm in our sample reflects the parameter space explored by M23, with this particular methodology being insensitive to larger radii – like those expected in Type IIn SNe. However, our analysis reveals a physically meaningful result: the rapid rise times observed in most events require both sufficient $M_{\rm CSM}$ and relatively compact radii ($\sim 6 \times 10^{14}$ cm median for $M_{\rm CSM} > 10^{-2.5}$ M$_\odot$) to rapidly and efficiently convert kinetic energy to radiation, accelerating the early light-curve evolution.

The high $M_{\rm CSM}$ ($\geq 10^{-1}$M$_\odot$) and $\dot{M}$ ($\geq 10^{-2}$ M$_\odot$yr^{-1}), we infer for a fraction of our sample (Figs 11a and 12a) likely produce distinctive spectroscopic signatures from compact and dense CSM, such as flash features typically lasting ≤ 1 week. While our study focuses on CSM shells with specific density profiles affecting early light curves ($\rho \propto r^{-2}$; Moriya et al. 2023b), Dessart & Jacobson-Galán (2023) demonstrate that different CSM configurations can produce similar photometric evolution while predicting different spectroscopic features (see Moriya 2023; Khatami & Kasen 2024; Jacobson-Galán et al. 2024a). Spectroscopy is required to aid in breaking these degeneracies as it becoming clear that large amounts of CSM represent a common phenomenon rather than exceptional cases (e.g. Förster et al. 2018; Hosseinzadeh et al. 2022, 2023; Kozyreva et al. 2022; Hiramatsu et al. 2023; Jacobson-Galán et al. 2023, 2024b; Jencson et al. 2023; Andrews et al. 2024; Chen et al. 2024; Irani et al. 2024; Li et al. 2024; Pessi et al. 2024; Shrestha et al. 2024; Xiang et al. 2024; Zimmerman et al. 2024; Rehemtulla et al. 2025).

For events with lower inferred $M_{\rm CSM}$ ($< 10^{-2.5}$ M$_\odot$), the impact of CSM on the early light curve is too weak to constrain $R_{\rm CSM}$. While many of these SNe are likely to possess non-negligible CSM, material at larger radii would likely not influence the early evolution, and would be too diffuse to influence the later light-curve evolution in a clearly discernible way unless the mass is extremely high (e.g. Irani et al. 2024).

A limitation of the approach from this work is that for the fastest rising events (≤ 1 d), which likely require dense, compact CSM to achieve such rapid evolution, our measured rise times would represent upper limits, unresolved fast rises might require more substantial $M_{\rm CSM}$ or closer and more compact CSM. While individual CSM parameters may have uncertainties due to model assumptions, observational constraints and scatter present in relationships, this frequency of substantial CSM in our volume corrected sample represents a robust statistical result, independent of the precise CSM parametrization. Our analysis is further constrained by confidence in classifications, an issue we explore in greater detail in Appendix A10.

6.4 Implications for mass-loss mechanisms

With a minimum $M_{\rm CSM}$, $10^{-2.5}$ M$_\odot$, and observationally supported fiducial values for $v_{\rm wind}$ and $R_{\rm CSM}$ of 10 km s^{-1} and 5×10^{14} cm, respectively, we find a characteristic $\dot{M}$ of 2×10^{-4} M$_\odot$yr^{-1}. This characteristic value is higher, by ~ 2 orders of magnitude, than values
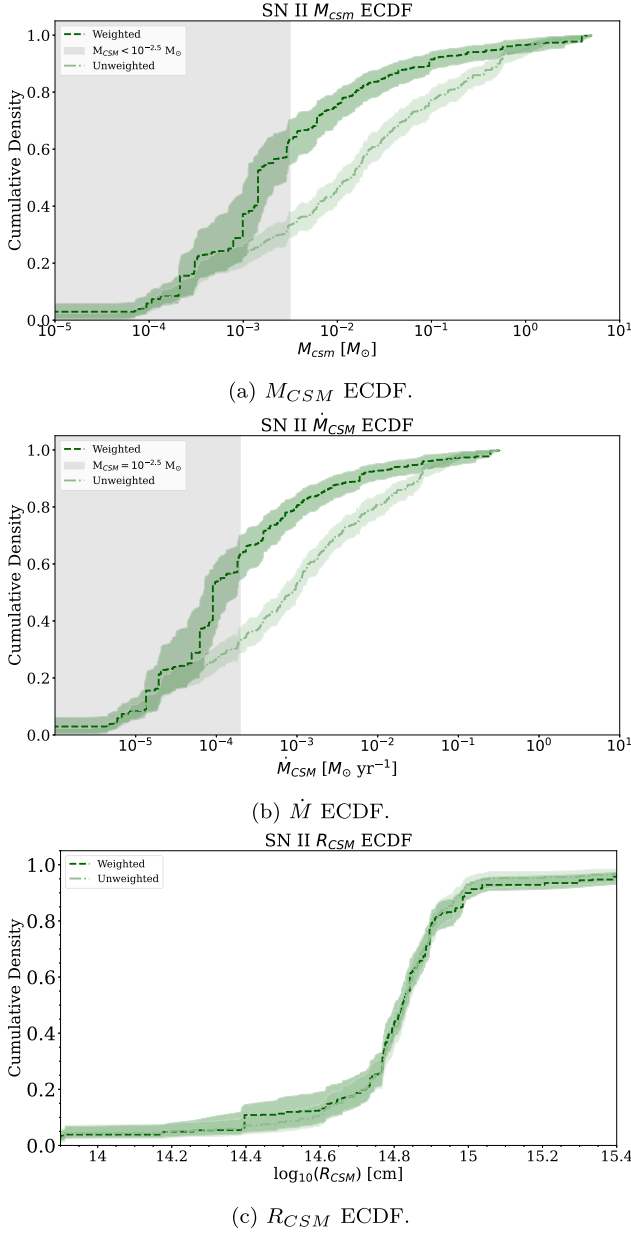
(a) M_{CSM} ECDF.

(b) $\dot{M}$ ECDF.

(c) R_{CSM} ECDF.

Figure 12. Type II weighted (dark green) and unweighted (light green) ECDF for M_{CSM}, $\dot{M}$, and R_{CSM}. We plot the 80 per cent CI for the weighted ECDF and the 95 per cent CI for the unweighted ECDF. For R_{CSM}, we exclude data where the corresponding $M_{\mathrm{CSM}} < 10^{-2.5}\,\mathrm{M}_\odot$ as we consider M_{CSM} lower than this to have a negligible effect on the observable parameters. The shaded region on the ECDFs for M_{CSM} and $\dot{M}$ are the same as applied in Figs 11(a) and (b).

inferred from observations of local group RSGs, e.g. $\dot{M} \sim 10^{-6}$ $\mathrm{M}_\odot\mathrm{yr}^{-1}$ (e.g. Vink, de Koter & Lamers 2001; Smith 2014; Beasor & Davies 2018; Beasor et al. 2020).

Our findings are instead closer to studies such as Morozova et al. (2017), Moriya et al. (2018), Bruch et al. (2021, 2023), Irani et al. (2024), and Jacobson-Galán et al. (2024a) that estimate $\dot{M}$ to be $\sim 10^{-4}$–10^{-1} $\mathrm{M}_\odot\mathrm{yr}^{-2}$ based on detailed analysis of spectroscopy and photometry of early SNe. Like Jacobson-Galán et al. (2024a), we find that Type II SNe exhibit a continuum of $\dot{M}$, representative of the heterogeneous morphology of light curves, with 46^{+5}_{-13} per cent

Table 7. Previous measurements of the mean AB peak absolute magnitudes for Type II SNe. Uncertainties are those reported in the study. Extinction refers to whether the magnitudes were corrected for MW and host extinction, or for MW extinction only with no host correction. Vol. refers to whether there is a volume correction applied to the statistic. Classification refers to how the final samples were selected, all choose to spectroscopically (spec) classify, with Anderson et al. (2014) performing some photometric (phot) typing to remove Type IIb, IIn and 1987A-like SNe. Survey refers to which surveys the samples belong to: CT – Cerro Tololo SN program. CTSN – Calán/Tololo SN. SOIRS – Optical and Infrared Supernova Survey. CATS – Carnegie Type II Supernova Program. CSP – Carnegie Supernova Program. C&T – Calán/Tololo Supernova Program. LOSS – Lick Observatory Supernova Search.

Reference	$M_{B,\mathrm{peak}}$ [mag]	$M_{V,\mathrm{peak}}$ [mag]	No.	Extinction	Vol.	Class Sys.	Surveys
Anderson et al. (2014)	–	-16.74 ± 1.01	68	MW & Host	No	Spec + Phot	CT; CTSN; SOIRS; CATS; CSP
Richardson et al. (2014)	-16.80 ± 0.37	–	74	MW & Host	Yes	Spec	ASC
Galbany et al. (2016)	-16.43 ± 1.19	-16.89 ± 0.98	51	MW	No	Spec	C&T; CTSN; SOIRS; CATS
de Jaeger et al. (2019)	-16.57 ± 1.14	-16.74 ± 0.92	23	MW	No	Spec	LOSS

of the corrected population having $\dot{M} \geq 1 \times 10^{-4}$ $M_\odot yr^{-1}$ in the last several decades before core-collapse.

Given a v_{wind} of 10 km s^{-1} and the minimum and maximum values of R_{CSM}, 10^{14}–10^{15} cm, we calculate the range of time-scales in which the material is removed to be 3–32 yr. The distinctly short time-scales of mass loss, compared to the lifespan of this evolutionary stage, further supports the need for a period of 'enhanced' mass-loss. We argue the higher rates of mass loss estimated from early photometry found here and by other studies (e.g. Irani et al. 2024; Silva-Farfán et al. 2024; Jacobson-Galán et al. 2024b) are probing the end-of-life mass-loss rather than the typical $\dot{M}$ of RSGs.

Any viable mass-loss mechanism must maintain sufficient CSM density at compact radii while preventing complete shell detachment. The mechanism must operate on time-scales consistent with our inferred $\dot{M}$ ($\geq 10^{-4}$ $M_\odot yr^{-1}$) and produce velocities that allow the material to remain within $R_{CSM} \leq 10^{15}$ cm. Higher ejection velocities or more extended distributions would result in CSM densities too low to effectively interact with the SN ejecta and SBO during the early light-curve evolution.

As an alternative to 'enhanced' $\dot{M}$ in the centuries before core-collapse, the dense chromosphere model of Fuller & Tsuna (2024) offers a compelling explanation for the apparent disparity between observed RSG mass-loss rates and those inferred from early SN evolution (see Fuller & Tsuna 2024). A chromosphere exists in approximate hydrostatic equilibrium, with significantly higher densities above the stellar surface than predicted by constant or β-law wind velocity models, despite maintaining $\dot{M}$ more consistent with local group RSG measurements (see fig. 4 in Fuller & Tsuna 2024). This model is able to naturally produce the rapid photometric and spectroscopic evolution observed in fast-rising SNe while preserving realistic progenitor properties. While our M_{CSM} estimates would remain largely unaffected, the inferred $\dot{M}$ would decrease substantially due to the significantly different velocity structure in Fuller & Tsuna (2024) compared to those used in M23. Thus, the chromosphere model represents a promising alternative to 'enhanced' $\dot{M}$, potentially resolving a tension between $\dot{M}$ measured from local RSGs and early SN evolution, though additional development is required to fully understand the impact of chromospheres on the photometric and spectroscopic evolution across diverse SN populations.

7 CONCLUSIONS

In this work, we have presented forced photometry and GP analysis of all spectroscopically classified H-rich SNe from the ZTF BTS, 1802 objects from 2018 May 1 to 2023 December 31, 981 of which pass various quality cuts outlined in BTS sample paper (Perley et al. 2020). We have modelled the light curves with GPR to return various empirical light-curve parameters, with a focus on the rise times of 639 Type II SNe. Using various light-curve parameters, we have created volume corrected (V_{max} method) distributions from the BTS sample, allowing us to confidently report the following main conclusions for a highly complete sample of 377 Type II SNe (excluding Type IIn and IIb SNe, and after a magnitude cut at $\leq$ 18.5 mag for completeness):

(i) We see large diversity in Type II light-curve demographics, but no clear separation in the luminosity-rise phase space. The predicted bimodality that appears when we measure the distributions of rise times, t_{25-75}, from the simulated light curves of Moriya et al. (2023b) is not seen in our observed light curves.

(ii) Based on the $1/V_{max}$ weighted sample of Type II SNe from this study, we find 36^{+5}_{-7} per cent of Type II SN progenitors have $M_{CSM} \geq 10^{-2.5}$ $M_\odot$ at the time of core-collapse. We find this is the minimum

amount of M_{CSM} needed to impact the observables like the rise time and peak magnitude, based on Moriya et al. (2023b) models.

(iii) For an assumed progenitor wind velocity of 10 km s^{-1}, a maximum CSM radius of $R_{CSM} \approx 5 \times 10^{14}$ cm and $M_{CSM} = 10^{-2.5}$ $M_\odot$, we estimate mass-loss rates of $\dot{M} \sim 2 \times 10^{-4}$ $M_\odot$ yr^{-1} for events showing CSM-affected light curves. We constrain the period of this to occur within the last 3–32 yr, consistent with recent findings from Bruch et al. (2021, 2023) and Jacobson-Galán et al. (2024a) which suggest 'enhanced' mass loss is a common feature of RSG evolution in the final decades before core-collapse.

This supports findings in recent literature that CSM interactions contribute significantly to the early light curve and are prevalent in a large set Type II SNe. While not ubiquitous across Type II SNe, we show possessing large amounts of CSM in common amongst Type II SNe progenitors. For the $\sim$ 36 per cent of Type II SNe (excluding Types IIn and IIb SNe) where CSM interactions dominate, we find that dense CSM both shortens the rise time to peak luminosity and enhances the early-time brightness. We have further highlighted the need to reconcile and address the disparity between light curve derived $\dot{M}$ values and $\dot{M}$ from RSG observations – which are typically larger by $\approx$ 2 orders of magnitudes than the rates inferred from local group RSG observations (e.g. van Loon et al. 2005; Mauron & Josselin 2011; Smith 2014; Beasor et al. 2020; Stroh et al. 2021; Strotjohann et al. 2024).

Mapping the true distribution of CSM properties and establishing robust connections between SNe and their progenitors requires deeper observations over longer baselines than currently available. The Vera Rubin Observatory, ZTF-III, and upcoming IR/UV missions will provide unprecedented multiwavelength coverage with the depth and cadence needed to probe fainter CSM signatures and earlier epochs, essential for reconstructing progenitor mass-loss histories and understanding how they shape the observed diversity of Type II SNe.

DATA AVAILABILITY

Alongside the upcoming publication, Miller et al. (in preparation), there will be a large data release o the ZTF P48 light curves used in this work.

The light curves and empirical properties measured for the SNe, as they relate to this work, can be found here: [https://doi.org/10.5281/zenodo.15229515].

Access to the public Bright Transient Survey sample explorer can be found here: [https://sites.astro.caltech.edu/ztf/bts/explorer.php].

REFERENCES

Aigrain S., Foreman-Mackey D., 2023, ARA&A, 61, 329
Ambikasaran S., Foreman-Mackey D., Greengard L., Hogg D. W., O'Neil M., 2015, IEEE Trans. Pattern Anal. Mach. Intell., 38, 252
Anderson J. P. et al., 2014, ApJ, 786, 67
Andrews J. E. et al., 2024, ApJ, 965, 85
Arcavi I. , 2017, in Alsabti A. W., Murdin P., eds, Handbook of Supernovae, Springer, Cham, p. 239
Arnett W. D., Meakin C., 2011, ApJ, 733, 78
Arnett W. D., Bahcall J. N., Kirshner R. P., Woosley S. E., 1989, ARA&A, 27, 629
Barker B. L., Harris C. E., Warren M. L., O'Connor E. P., Couch S. M., 2022, ApJ, 934, 67
Barker B. L., O'Connor E. P., Couch S. M., 2023, ApJ, 944, L2
Beasor E. R., Davies B., 2018, MNRAS, 475, 55
Beasor E. R., Davies B., Smith N., van Loon J. T., Gehrz R. D., Figer D. F., 2020, MNRAS, 492, 5994
Bellm E. C. et al., 2019a, PASP, 131, 018002
Bellm E. C. et al., 2019b, PASP, 131, 068003
Benson P. J. et al., 1994, AJ, 107, 1453
Blagorodnova N. et al., 2018, PASP, 130, 035003
Blinnikov S. I., Eastman R., Bartunov O. S., Popolitov V. A., Woosley S. E., 1998, ApJ, 496, 454
Blinnikov S., Lundqvist P., Bartunov O., Nomoto K., Iwamoto K., 2000, ApJ, 532, 1132
Blinnikov S. I., Röpke F. K., Sorokina E. I., Gieseler M., Reinecke M., Travaglio C., Hillebrandt W., Stritzinger M., 2006, A&A, 453, 229
Bostroem K. A. et al., 2023, ApJ, 956, L5
Bruch R. J. et al., 2021, ApJ, 912, 46
Bruch R. J. et al., 2023, ApJ, 952, 119
Cardelli J. A., Clayton G. C., Mathis J. S., 1989, ApJ, 345, 245
Catchpole R. M., 1989, Highlights Astron., 8, 185
Chen T.-W. et al., 2025, ApJ, 983, 86
Chen X. et al., 2024, ApJ, 971, L2
Chevalier R. A., 1992, ApJ, 394, 599
Chevalier R. A., 2012, ApJ, 752, L2
Chevalier R. A., Fransson C., 2008, ApJ, 683, L135
Chevalier R. A., Irwin C. M., 2011, ApJ, 729, L6
Chieffi A., Domínguez I., Höflich P., Limongi M., Straniero O., 2003, MNRAS, 345, 111
Coughlin M. W. et al., 2023, ApJS, 267, 31
Das K. K. et al., 2025, PASP, 137, 044203
Das S., Ray A., 2017, ApJ, 851, 138
Davies B., Plez B., Petrault M., 2022, MNRAS, 517, 1483
Davis S. et al., 2019, ApJ, 887, 4
de Jaeger T. et al., 2018, MNRAS, 476, 4592
de Jaeger T. et al., 2019, MNRAS, 490, 2799
De K. et al., 2020, ApJ, 905, 58
Dekany R. et al., 2020, PASP, 132, 038001
Dessart L., Audit E., Hillier D. J., 2015, MNRAS, 449, 4304
Dessart L., Hillier D. J., Audit E., 2017, A&A, 605, A83
Dessart L., Jacobson-Galán W. V., 2023, A&A, 677, A105
Dong Y. et al., 2024, ApJ, 977, 254
Duev D. A., van der Walt S. J., 2021, preprint (arXiv:2111.12142)
Duev D. A. et al., 2019, MNRAS, 489, 3582
Eldridge J. J., Tout C. A., 2004, MNRAS, 353, 87
Eldridge J. J., Izzard R. G., Tout C. A., 2008, MNRAS, 384, 1109
Eldridge J. J., Xiao L., Stanway E. R., Rodrigues N., Guo N. Y., 2018, Publ. Astron. Soc. Aust., 35, e049
Fang Q., Maeda K., Ye H., Moriya T. J., Matsumoto T., 2025, ApJ, 978, 35
Fassia A. et al., 2000, MNRAS, 318, 1093
Förster F. et al., 2018, Nat. Astron., 2, 808
Fransson C., Gilmozzi R., Groeningsson P., Hanuschik R., Kjaer K., Leibundgut B., Spyromilio J., 2007, The Messenger, 127, 44
Fransson C. et al., 2014, ApJ, 797, 118
Fraser M. et al., 2013, ApJ, 779, L8
Fremling C. et al., 2020, ApJ, 895, 32
Fuller J., 2017, MNRAS, 470, 1642
Fuller J., Tsuna D., 2024, Open J. Astrophys., 7, 47
Gal-Yam A., 2017, W. Alsabti A., Murdin P., eds, Handbook of Supernovae, Springer, Cham, p. 195
Gal-Yam A. et al., 2014, Nature, 509, 471
Galbany L. et al., 2016, AJ, 151, 33
Gall E. E. E. et al., 2015, A&A, 582, A3
Goldberg J., 2022, Understanding Type II-Plateau Supernovae and the Red Supergiants that Cause Them, UC Santa Barbara, Retrieved from https://escholarship.org/uc/item/65m867f0.
González-Gaitán S. et al., 2015, MNRAS, 451, 2212
Graham M. J. et al., 2019, PASP, 131, 078001
Graur O., Bianco F. B., Modjaz M., Shivvers I., Filippenko A. V., Li W., Smith N., 2017, ApJ, 837, 121
Groh J. H., 2014, A&A, 572, L11
Gutiérrez C. P. et al., 2017a, ApJ, 850, 89
Gutiérrez C. P. et al., 2017b, ApJ, 850, 90
Helou G., Madore B. F., Schmitz M., Bicay M. D., Wu X., Bennett J., 1991, in Albrecht M. A., Egret D., eds, Astrophysics and Space Science LibraryVol. 171, Databases and On-line Data in Astronomy. Springer, Dordrecht, p. 89
Hillier D. J., Dessart L., 2012, MNRAS, 424, 252
Hiramatsu D. et al., 2021, ApJ, 913, 55
Hiramatsu D. et al., 2023, ApJ, 955, L8
Hiramatsu D., Berger E., Gomez S., Blanchard P. K., Kumar H., Athukoralalage W., 2024, preprint (arXiv:2411.07287)
Hosseinzadeh G. et al., 2018, ApJ, 861, 63
Hosseinzadeh G. et al., 2022, ApJ, 935, 31
Hosseinzadeh G. et al., 2023, ApJ, 953, L16
Humphreys R. M., Helmel G., Jones T. J., Gordon M. S., 2020, AJ, 160, 145
Irani I. et al., 2024, ApJ, 970, 96
Jacobson-Galán W. V. et al., 2022, ApJ, 924, 15
Jacobson-Galán W. V. et al., 2023, ApJ, 954, L42
Jacobson-Galán W. V. et al., 2024a, ApJ, 970, 189
Jacobson-Galán W. V. et al., 2024b, ApJ, 972, 177

Jencson J. E. et al., 2023, ApJ, 952, L30

Jerkstrand A., Ergon M., Smartt S. J., Fransson C., Sollerman J., Taubenberger S., Bersten M., Spyromilio J., 2014, A&A, 573, A12

Kangas T. et al., 2022, MNRAS, 516, 1193

Kasliwal M. M. et al., 2019, PASP, 131, 038003

Khatami D. K., Kasen D. N., 2024, ApJ, 972, 140

Kiewe M. et al., 2012, ApJ, 744, 10

Kim Y. L. et al., 2022, PASP, 134, 024505

Kleiser I. K. W. et al., 2011, MNRAS, 415, 372

Kozyreva A., Klencki J., Filippenko A. V., Baklanov P., Mironov A., Justham S., Chiavassa A., 2022, ApJ, 934, L31

Kulkarni S. R. et al., 2023, preprint (arXiv:2111.15608)

Langer N., 2012, ARA&A, 50, 107

Li G. et al., 2024, Nature, 627, 754

Lyman J. D., Bersier D., James P. A., 2014, MNRAS, 437, 3848

Malmquist K. G., 1920, Medd. fran Lunds Astron. Observ. Ser. I, 96, 1

Masci F. J. et al., 2019, PASP, 131, 018003

Masci F. J. et al., 2023, preprint (arXiv:2305.16279)

Maund J. R. et al., 2021, MNRAS, 503, 312

Mauron N., Josselin E., 2011, A&A, 526, A156

Medler K. et al., 2022, MNRAS, 513, 5540

Morag J., Sapir N., Waxman E., 2023, MNRAS, 522, 2764

Moriya T. J., 2023, MNRAS, 524, 5309

Moriya T. J., Singh A., 2024, PASJ, 76, 1050

Moriya T., Tominaga N., Blinnikov S. I., Baklanov P. V., Sorokina E. I., 2011, MNRAS, 415, 199

Moriya T. J., Förster F., Yoon S.-C., Gräfener G., Blinnikov S. I., 2018, MNRAS, 476, 2840

Moriya T., Subrayan B. M., Milisavljevic D., Blinnikov S. I., 2023a, PASJ, 75, 634

Moriya T. J., Subrayan B. M., Milisavljevic D., Blinnikov S. I., 2023b, PASJ, 75, 634

Morozova V., Piro A. L., Renzo M., Ott C. D., Clausen D., Couch S. M., Ellis J., Roberts L. F., 2015, ApJ, 814, 63

Morozova V., Piro A. L., Renzo M., Ott C. D., 2016, ApJ, 829, 109

Morozova V., Piro A. L., Valenti S., 2017, ApJ, 838, 28

Morozova V., Piro A. L., Valenti S., 2018, ApJ, 858, 15

Morozova V., Piro A. L., Fuller J., Van Dyk S. D., 2020, ApJ, 891, L32

Nakar E., Sari R., 2010, ApJ, 725, 904

Nyholm A. et al., 2020, A&A, 637, A73

Ofek E. O. et al., 2010, ApJ, 724, 1396

Oke J. B., Gunn J. E., 1982, PASP, 94, 586

Pastorello A. et al., 2012, A&A, 537, A141

Patterson M. T. et al., 2019, PASP, 131, 018001

Pearson J. et al., 2023, ApJ, 945, 107

Perley D. A. et al., 2020, ApJ, 904, 35

Pessi P. J. et al., 2019, MNRAS, 488, 4239

Pessi P. J. et al., 2023, MNRAS, 523, 5315

Pessi P. J. et al., 2025, A&A, 695, A142

Pessi T. et al., 2024, A&A, 688, L28

Podsiadlowski P., Hsu J. J. L., Joss P. C., Ross R. R., 1993, Nature, 364, 509

Popov D. V., 1993, ApJ, 414, 712

Prentice S. J. et al., 2020, MNRAS, 499, 1450

Ransome C. L., Habergham-Mawson S. M., Darnley M. J., James P. A., Filippenko A. V., Schlegel E. M., 2021, MNRAS, 506, 4715

Rasmussen C. E., Bousquet O., von Luxburg U., Rätsch G., Williams C. K. I., 2004, Gaussian Processes in Machine Learning. Springer, Berlin, Heidelberg, p. 3

Rehemtulla N. , et al., 2025, ApJ, 985, 241

Reynolds T. M. et al., 2020, MNRAS, 493, 1761

Richardson D., III R. L. J., Wright J., Maddox L., 2014, AJ, 147, 118

Richmond M. W., Treffers R. R., Filippenko A. V., Paik Y., Leibundgut B., Schulman E., Cox C. V., 1994, AJ, 107, 1022

Rigault M. et al., 2019, A&A, 627, A115

Rodrigo C., Solano E., 2020, in Contributions to the XIV. 0 Scientific Meeting (virtual) of the Spanish Astronomical Society. p. 182, available at: https://www.sea-astronomia.es/reunion-cientifica-2020

Rodrigo C. et al., 2024, A&A, 689, A93

Rubin A. et al., 2016, ApJ, 820, 33

Salpeter E. E., 1955, ApJ, 121, 161

Sana H. et al., 2012, Science, 337, 444

Sánchez-Sáez P. et al., 2021, AJ, 161, 141

Sanders N. E. et al., 2015, ApJ, 799, 208

Schaeffer R., Cassé M., Mochkovitch R., Cahen S., & Nomoto K., 1988, in Atmospheric Diagnostics of Stellar Evolution: Chemical Peculiarity, Mass Loss, and Explosion. Springer, Berlin, Heidelberg, p. 438

Schlafly E. F., Finkbeiner D. P., 2011, ApJ, 737, 103

Schlegel E. M., 1990, MNRAS, 244, 269

Schmidt M., 1968, ApJ, 151, 393

Shivvers I. et al., 2017, PASP, 129, 054201

Shrestha M. et al., 2024, ApJ, 972, L15

Silva-Farfán J. et al., 2024, ApJ, 969, 57

Singh A. et al., 2019, ApJ, 882, L15

Singh A. et al., 2024, ApJ, 975, 132

Sit T. et al., 2023, ApJ, 959, 142

Smartt S. J., 2009, ARA&A, 47, 63

Smartt S. J., 2015, Publ. Astron. Soc. Aust., 32, e016

Smith N., 2014, ARA&A, 52, 487

Smith N., 2017a, in Alsabti A. W., Murdin P., eds, Handbook of Supernovae, Springer, Cham, p. 403

Smith N., 2017b, Phil. Trans. R. Soc. A, 375, 20160268

Smith N., Arnett W. D., 2014, ApJ, 785, 82

Smith N., Chornock R., Silverman J. M., Filippenko A. V., Foley R. J., 2010, ApJ, 709, 856

Stroh M. C. et al., 2021, ApJ, 923, L24

Strotjohann N. L. et al., 2021, ApJ, 907, 99

Strotjohann N. L. et al., 2024, ApJ, 960, 72

Suntzeff N. B., 1997, preprint (arXiv:astro-ph/9707324)

Suntzeff N. B., Phillips M. M., Elias J. H., Depoy D. L., Walker A. R., 1992, ApJ, 384, L33

Suntzeff N., Bouchet P., 1990, AJ, 99, 650

Svirski G., Nakar E., Sari R., 2012, ApJ, 759, 108

Taddia F. et al., 2013, A&A, 555, A10

Theureau G. et al., 2005, A&A, 430, 373

Theureau G., Hanski M. O., Coudreau N., Hallet N., Martin J. M., 2007, A&A, 465, 71

Thévenot M., 2020, Res. Notes Am. Astron. Soc., 4, 243

Thornton I., Villar V. A., Gomez S., Hosseinzadeh G., 2024, Res. Notes Am. Astron. Soc., 8, 48

Tinyanont S. et al., 2021, Nat. Astron., 5, 544

Tinyanont S. et al., 2022, MNRAS, 512, 2777

Tominaga N., Morokuma T., Blinnikov S. I., Baklanov P., Sorokina E. I., Nomoto K., 2011, ApJS, 193, 20

Valenti S. et al., 2016, MNRAS, 459, 3939

Valerin G. et al., 2022, MNRAS, 513, 4983

van der Walt S. J., Crellin-Quick A., Bloom J. S., 2019, J. Open Source Softw., 4, 1247

Van Dyk S. D., 2017, Phil. Trans. R. Soc. Lond. Ser. A, 375, 20160277

van Loon J. T., Cioni M. R. L., Zijlstra A. A., Loup C., 2005, A&A, 438, 273

Villar V. A., Berger E., Metzger B. D., Guillochon J., 2017, ApJ, 849, 70

Villar V. A. et al., 2019, ApJ, 884, 83

Vink J. S., 2008, New Astron. Rev., 52, 419

Vink J. S., Gautham S. N., 2023, A&A, 678, L3

Vink J. S., de Koter A., Lamers H. J. G. L. M., 2001, A&A, 369, 574

Warwick B. et al., 2025, MNRAS, 536, 3588

Woosley S. E., 1988, ApJ, 330, 218

Woosley S. E., Eastman R. G., Weaver T. A., Pinto P. A., 1994, ApJ, 429, 300

Wu C. O., 1997, J. Multivariate Anal., 61, 38

Wu S., Fuller J., 2021, ApJ, 906, 3

Xiang D. et al., 2023, MNRAS, 520, 2965

Xiang D. et al., 2024, ApJ, 969, L15

Yang S. et al., 2021, A&A, 655, A90

Yaron O. et al., 2017, Nat. Phys., 13, 510

Young T. R., 2004, ApJ, 617, 1233

Zackay B., Ofek E. O., Gal-Yam A., 2016, ApJ, 830, 27

Zapartas E. et al., 2019, A&A, 631, A5

Zapartas E., de Mink S. E., Justham S., Smith N., Renzo M., de Koter A., 2021, A&A, 645, A6

Zimmerman E., Schulze S., Johansson J., Yang Y., Perley D., Bruch R., Gal-Yam A., 2021, Transient Name Server AstroNote, 91, 1

Zimmerman E. A. et al., 2024, Nature, 627, 759

APPENDIX A: SUPPLEMENTARY MATERIAL

A1 Heavily host-extinguished

Table A1 contains significantly dust-extinguished Type II SNe we identify in our sample. These events are characterized by distinctly red colours, $(g-r)_{g,\max} \geq 0.25$ mag, at peak and moderate rise times, $t_{25\_75} \leq 20$ d, placing them in a unique region of parameter space as illustrated in Fig. 2. We correct for host extinction using $(g-r)_{g,\max}$ and apply this correction to these SNe only, as described in Section 2.4.

A2 Rise time recovery

To assess the impact of the sampling function on our GPR measurements, we conducted a systematic resampling experiment using well-sampled light curves with well-constrained t_{25_75} values. This involved taking thoroughly observed events (e.g. ZTF18aacnlxz/SN 2020aavr) and resampling their light curves (simulating alternative sampling functions) to match the observation cadence of more sparsely observed light curves in our sample. Fig. A1 illustrates the resulting distribution of measured rise times across different intrinsic t_{25_75} values.

Our analysis demonstrates that the GPR process reliably distinguishes between fast-rising ($t_{25\_75} \leq 5$ d) and slowerrising ($t_{25\_75} > 5$ d) events. For the fastest risers (t_{25_75} between 1–2 d), we observe substantial uncertainty with a spread of ≈ 0.7 dex. This improves to ≈ 0.4 dex for moderate risers (t_{25_75} between 3–5 d) and further to ≈ 0.2 dex for slower rising events ($t_{25\_75} > 5$ d).

A3 Sample redshift distribution

In Fig. A2, we show the distribution of redshift, z, across our SN sample. The upper panel shows the z distribution for our full data set, and the lower panel displays the highly complete (~ 95 per cent) sample limited to events with peak apparent magnitudes $m_{\mathrm{peak}} \leq 18.5$ mag.

A4 Peak colours

In Figs A3(a)–(f), we present the KDE distributions (left) and ECDFs (*right*) of peak $g-r$ colours ($(g-r)_{g,\max}$) for Type II, Type IIn and Type IIb SNe. The panels display distributions for standard Type II (top), Type IIn (middle), and Type IIb (bottom) SNe. We show various statistical quantities for each distribution in Table 4.

A5 M23 luminosity rise

Fig. A4 shows the distribution of t_{25_75} versus $M_{g,\mathrm{peak}}$ for the theoretical light-curve grid from M23. We present 10 000 model points using the same $V_{\max} \times M_{\mathrm{ZAMS}}^{-2.35}$ weighting scheme applied in Fig. 8, which accounts for both observational selection effects and the IMF (e.g. Salpeter 1955). The top panel colour-codes data by $\dot{M}$, while the bottom panel uses R_{CSM}.

This visualization reveals how CSM properties strongly influence the distribution of SNe in the t_{25_75}–$M_{g,\mathrm{peak}}$ plane. Fast risers ($t_{25\_75} \leq$

5 d) typically have confined, dense CSM characterized by higher $\dot{M}$ and smaller R_{CSM}, producing moderately more luminous peaks. In contrast, slower risers ($t_{25\_75} > 5$ d) typically exhibit less confined and less dense CSM with lower overall M_{CSM} values and larger R_{CSM}. Notably, even within the slower rising population, the most luminous events still require substantial CSM masses, confirming that CSM mass remains a fundamental driver of peak luminosity across the distribution.

The clear separation between these populations emerges naturally from the underlying physics rather than from arbitrary parameter choices, suggesting fundamental differences in mass-loss mechanisms or progenitor structures. This bimodality provides valuable context for interpreting the observed distribution of Type II SNe in our sample.

A6 $M_{\mathrm{Fe,Core}}$ measurements

We extend the predictive capabilities of multi-output GPR extend to estimating the iron core mass, $M_{\mathrm{Fe,Core}}$, of the progenitor through equation (A1), which exploits a tight correlation between $M_{\mathrm{Fe,Core}}$ and the plateau luminosity at 50 d in simulated Type IIP light curves (e.g. Barker et al. 2022, 2023). The theoretical correlation indicates that more massive stellar cores lead to more energetic and luminous SNe, notably enhancing the bolometric luminosity during the plateau phase at approximately 50 d post-explosion (Barker et al. 2022). To quantify this relationship, we utilie the bolometric plateau luminosity at 50 d, $L_{bol,50d}$. The plateau length is measured by analysing the gradient along the light curve and identifying significant changes in the slope. The ZTF g- and r-band magnitudes are measured at 50 d after the plateau onset. A bolometric correction is then applied to convert these magnitudes into bolometric luminosity – we adopt the methodology described by Lyman, Bersier & James (2014).

$$\frac{M_{\mathrm{Fe,Core}}}{\mathrm{M_\odot}} = 0.0978 \times \left(\frac{L_{\mathrm{bol,50\,d}}}{10^{42}\ \mathrm{erg\ s^{-1}}} \right) + 1.29 \qquad (A1)$$

The KDE distribution for $M_{\mathrm{Fe,Core}}$, Fig. A5, shows a sharp cut-off at 1.3 M$_\odot$, reflecting the lower limit of iron core masses in the models from which the correlation was derived (Barker et al. 2022). Since the KDE smoothing kernel could not properly handle this abrupt transition, we truncate the distribution at 1.3 M$_\odot$ and normalize the probability density to unity.

The weighted mean $M_{\mathrm{Fe,Core}}$ of 1.36 ± 0.01 M$_\odot$ is consistent with the mean found in Barker et al. (2022, 2023) of 1.4 ± 0.05 M$_\odot$ to within 1σ – see Table A2. The distribution appears to be in agreement with the distribution created by Barker et al. (2022, 2023), as they find a range in $M_{\mathrm{Fe,Core}}$ (1.3–1.5 ± 0.05 M$_\odot$) after applying equation (A1) to CCSN samples from Anderson et al. (2014) and Gutiérrez et al. (2017a,b).

While this correlation provides a useful estimate of the core mass, it assumes a direct relationship between core mass and explosion energy that, in reality, may be complicated by ejecta properties (mass and H-richness). Higher ejecta masses or more H-richness can extend and diminish the plateau luminosity independent of core mass (e.g. Goldberg 2022). The use of luminosity at 50 d may be particularly sensitive to hydrogen envelope mass variations, as it assumes complete H retention (e.g. Goldberg 2022; Fang et al. 2025). A more robust approach might utilie the luminosity at half the plateau duration, which better accounts for diversity in envelope masses and better isolates the core mass contribution to the light -curve evolution (Fang et al. 2025).

Table A1. Properties of heavily dust-extinguished Type II SNe, identified by their red colours, $(g-r)_{g,\max} \geq 0.25$ mag, and moderate rise times, $t_{25\_75} \leq 20$ d, as shown in Fig. 2. Table contains: ZTF object name; TNS name; spectroscopic classification; redshift; $M_{g,\text{peak}}$ in ZTF g at rest-frame and uncertainty; t_{25_75} rise time [d] in ZTF g at rest-frame wavelength and uncertainty; $g-r$ colour at ZTF g peak time and uncertainty; and host galaxy extinction in ZTF g band, method described in Section 2.4.

ZTF	TNS ID	Type	z	$M_{g,\text{peak}}$[mag]	t_{25_75}[d]	$(g-r)_{g,\max}$[mag]	A_g^{host} [mag]
ZTF18abdbysy	2018cyg	II	0.01127	-14.40 ± 0.02	1.70 ± 0.18	0.71 ± 0.03	2.38
ZTF18abvvmdf	2018gts	II	0.029597	-16.70 ± 0.02	2.00 ± 0.14	0.59 ± 0.03	1.97
ZTF19aamkmxv	2019bxq	IIn	0.014	-16.66 ± 0.02	3.41 ± 0.16	0.77 ± 0.02	2.61
ZTF19aamvape	2019cjx	II	0.03	-17.69 ± 0.02	8.43 ± 0.39	0.30 ± 0.02	1.01
ZTF19aayrosj	2019hrb	II	0.015064	-15.86 ± 0.02	1.83 ± 0.14	0.27 ± 0.03	0.90
ZTF19abgfuhh	2019lgc	IIb	0.0354	-17.35 ± 0.02	3.99 ± 0.19	0.37 ± 0.03	1.26
ZTF19abxtcio	2019pof	IIb	0.0155	-15.79 ± 0.02	14.30 ± 0.68	0.46 ± 0.03	1.57
ZTF20aaetrle	2020sy	II	0.02	-16.99 ± 0.02	6.97 ± 0.68	0.47 ± 0.04	1.60
ZTF20aaurfwa	2020hem	IIn	0.0935	-20.37 ± 0.01	16.86 ± 0.51	0.32 ± 0.01	1.09
ZTF20abfcrzj	2020mob	IIb	0.023244	-16.86 ± 0.06	10.01 ± 0.68	0.26 ± 0.08	0.87
ZTF20abpmqnr	2020qmj	IIn	0.022	-18.53 ± 0.01	7.47 ± 0.18	0.42 ± 0.01	1.41
ZTF20abwzqzo	2020sbw	IIb	0.023033	-16.64 ± 0.07	7.97 ± 2.60	0.38 ± 0.10	1.27
ZTF20aclkhnm	2020xql	II	0.036	-17.07 ± 0.04	12.93 ± 1.61	0.56 ± 0.06	1.90
ZTF20acnzkxb	2020ykd	II	0.02690421	-16.95 ± 0.01	5.65 ± 0.28	0.40 ± 0.02	1.33
ZTF20acpgokr	2020yzi	II	0.027	-16.72 ± 0.02	2.08 ± 0.15	0.34 ± 0.03	1.15
ZTF20acrzwvx	2020aatb	II	0.009954	-16.41 ± 0.01	7.70 ± 0.52	0.45 ± 0.02	1.51
ZTF20actqnhg	2020aaxf	IIb	0.014813	-16.55 ± 0.02	5.01 ± 0.35	0.38 ± 0.03	1.27
ZTF20acvevsn	2020abqw	II	0.01417	-14.96 ± 0.02	1.73 ± 0.22	0.42 ± 0.04	1.42
ZTF21aajgdeu	2021cjd	II	0.027929	-16.71 ± 0.04	1.76 ± 0.19	0.36 ± 0.05	1.22
ZTF21aakupth	2021cvd	IIn	0.023483	-16.11 ± 0.02	4.33 ± 0.32	0.52 ± 0.03	1.76
ZTF21aamwqim	2021dru	II	0.025878	-16.51 ± 0.05	4.17 ± 0.70	0.46 ± 0.07	1.57
ZTF21aavuqzr	2021kat	IIn	0.1013	-20.24 ± 0.01	16.78 ± 0.50	0.35 ± 0.01	1.19
ZTF21aaydxoo	2021kwc	IIn	0.021759	-17.53 ± 0.01	4.85 ± 0.15	0.59 ± 0.01	1.99
ZTF21aayfnjz	2021kww	II	0.023	-17.52 ± 0.01	6.31 ± 0.13	0.31 ± 0.02	1.04
ZTF21abfoyac	2021pni	II	0.033	-18.27 ± 0.01	7.40 ± 0.25	0.38 ± 0.01	1.27
ZTF21abujgmr	2021wrr	IIn	0.048	-17.95 ± 0.01	6.86 ± 0.37	0.44 ± 0.01	1.47
ZTF21abviabc	2021wyn	II	0.053467	-18.20 ± 0.02	3.32 ± 0.39	0.75 ± 0.02	2.54
ZTF21abyqrli	2021ybc	IIb	0.02925	-17.29 ± 0.09	6.15 ± 1.26	0.29 ± 0.04	0.99
ZTF22aagvxjc	2022iep	IIn	0.025	-17.00 ± 0.01	16.40 ± 0.60	0.28 ± 0.01	0.95
ZTF22aalorla	2022lix	II	0.06804	-18.66 ± 0.01	5.52 ± 0.13	0.46 ± 0.01	1.54
ZTF22aamjqvc	2018elp	IIb	0.030089	-17.57 ± 0.01	5.56 ± 0.20	0.29 ± 0.02	0.99
ZTF22aaotgrc	2022ngb	IIb	0.00965	-16.18 ± 0.02	6.96 ± 0.13	0.66 ± 0.03	2.23
ZTF22aapqaqe	2022npv	II	0.025177	-17.32 ± 0.01	3.21 ± 0.12	0.46 ± 0.02	1.54
ZTF22aawptbl	2022pzh	II	0.045	-18.20 ± 0.02	5.79 ± 0.48	0.44 ± 0.02	1.49
ZTF22ablvnwa	2022xae	IIb	0.045229	-18.09 ± 0.04	4.64 ± 0.57	0.26 ± 0.05	0.87
ZTF22abnejmu	2022ycs	II	0.01	-15.50 ± 0.02	9.14 ± 1.46	0.48 ± 0.02	1.61
ZTF22abssiet	2022zmb	II	0.01449	-15.41 ± 0.02	1.73 ± 0.11	0.25 ± 0.03	0.85
ZTF23aaawbsc	2023aew	IIb	0.025	-18.55 ± 0.03	7.41 ± 0.22	0.30 ± 0.03	1.01
ZTF23aaesmsf	2023fsc	IIb	0.02	-17.81 ± 0.01	11.13 ± 0.41	0.34 ± 0.02	1.13
ZTF23aazqmwp	2023qec	II	0.02079	-17.50 ± 0.01	6.88 ± 0.21	0.26 ± 0.02	0.88
ZTF23abjrolf	2023uvh	II	0.02676	-16.69 ± 0.07	4.81 ± 1.15	0.46 ± 0.10	1.54

Table A2. Mean and median of the volumecorrected KDE for $M_{\text{Fe,Core}}$ in the final sample. Uncertainties reported here are the standard deviation on the bootstrapped values.

Parameter	Units	Mean	25th percentile	50th percentile	75th percentile	Range	No.
			Weighted				
$M_{\text{Fe,Core}}$	$M_\odot$	1.36 ± 0.01	$1.31^{+0.02}_{-0.01}$	1.34 ± 0.01	$1.38^{+0.01}_{-0.04}$	[1.30,3.31]	354
			Unweighted				
$M_{\text{Fe,Core}}$	$M_\odot$	1.49 ± 0.01	$1.38^{+0.02}_{-0.01}$	1.45 ± 0.01	$1.53^{+0.01}_{-0.02}$	–	–

Note. The range reported is the 5th and 95th percentiles to remove outliers beyond the limits of the original data set.

A7 M23 relations

$$\log_{10}(U) = C_0 + C_1 \times V + C_2 \times W + C_3 \times X \\ + C_4 \times Y + C_5 \times Z \tag{A2}$$

$$\log_{10}(U) = C_0 + C_1 \times V^2 + C_2 \times (V \times W) + C_3 \\ \times (V \times X) + C_4 \times (V \times Y) + C_5 \times (V \times Z) \\ + C_6 \times W^2 + C_7 \times (W \times X) \\ + C_8 \times (W \times Y) + C_9 \times (W \times Z) + C_{10} \times X^2 \\ + C_{11} \times (X \times Y) + C_{12} \times (X \times Z) + C_{13} \\ \times Y^2 + C_{14} \times (Y \times Z) + C_{15} \times Z^2 \tag{A3}$$

$$\log_{10}(U) = C_0 + C_1 \times V^3 + C_2 \times (V^2 \times W) + C_3 \times (V \times W^2) \\ + C_4 \times W^3 + C_5 \times (V^2 \times X) + C_6 \times (V \times W \times X) \\ + C_7 \times (W^2 \times X) + C_8 \times (V \times X^2) + C_9 \times (W \times X^2) \\ + C_{10} \times X^3 + C_{11} \times (V^2 \times Y) + C_{12} \times (V \times W \times Y) \\ + C_{13} \times (W^2 \times Y) \\ + C_{14} \times (V \times X \times Y) + C_{15} \times (W \times X \times Y) \\ + C_{16} \times (X^2 \times Y) + C_{17} \times (V \times Y^2) \\ + C_{18} \times (W \times Y^2) + C_{19} \times (X \times Y^2) \\ + C_{20} \times Y^3 + C_{21} \times (V^2 \times Z) + C_{22} \times (V \times W \times Z) \\ + C_{23} \times (W^2 \times Z) + C_{24} \times (V \times X \times Z) + C_{25} \\ \times (W \times X \times Z) + C_{26} \times (X^2 \times Z) \\ + C_{27} \times (V \times Y \times Z) + C_{28} \times (W \times Y \times Z) \\ + C_{29} \times (X \times Y \times Z) + C_{30} \times (Y^2 \times Z) \\ + C_{31} \times (V \times Z^2) + C_{32} \times (W \times Z^2) \\ + C_{33} \times (X \times Z^2) + C_{34} \times (Y \times Z^2) + C_{35} \times Z^3 \tag{A4}$$

For $M_{\rm CSM}$, $U = M_{\rm CSM}$, $V = M_{g,\rm peak}$, $W = \log_{10}(t_{20\_60})$, $X = \log_{10}(t_{60\_90})$, $Y = (g-r)_{g,\rm max}$, and $Z = M_{g,10d}$.

For $R_{\rm CSM}$, $U = R_{\rm CSM}$, $V = M_{g,\rm peak}$, $W = \log_{10}(t_{20\_50})$, $X = \log_{10}(t_{50\_80})$, $Y = (g-r)_{g,\rm max}$, and $Z = M_{g,5d}$.

A8 M23 radial extent predictions

Fig. A6 shows the multivariate analysis comparing our polynomial regression-predicted CSM radial extent values (y-axis) against the corresponding M23 model values (x-axis), following an approach similar to Fig. 10. This systematic evaluation examines the performance of polynomial fits across different degrees (first, second, and third order) and specific parameter regimes to determine the optimal method for characterizing this relationship. Unlike our $M_{\rm CSM}$ analysis, this investigation of $R_{\rm CSM}$ is restricted to M23 models with $M_{\rm CSM} \geq 1 \times 10^{-2.5}$ M$_\odot$, which Section 5.1 identifies as the threshold above which CSM significantly influences both $M_{g,\rm peak}$ and t_{25_75}. The results demonstrate that $R_{\rm CSM}$ can only be reliably constrained for events with substantial $M_{\rm CSM}$.

A9 M23 $M_{\rm CSM}$ lower limit

Accurate measurements of $R_{\rm CSM}$ becomes challenging when $M_{\rm CSM}$ is insufficient to significantly influence observables such as $M_{g,\rm peak}$ and t_{25_75}. To establish a critical threshold below which CSM becomes virtually undetectable in early light curves, we systematically analysed how variations in key physical parameters – $\dot{M}$, $R_{\rm CSM}$, and β – affect observable properties.

We systematically varied these parameters while holding other key physical parameters constant (e.g. nickel mass). Our investigation revealed that when $M_{\rm CSM}$ falls below approximately $10^{-2.5}$ M$_\odot$, the CSM becomes too diffuse to meaningfully influence early lightcurve evolution. This threshold is evidenced by minimal variations in $M_{g,\rm peak}$ below $10^{-2.5}$ M$_\odot$ and increasingly significant variations above this mass – a pattern consistent across all progenitor masses. At this critical point, we observe a transition to a regime where CSM interaction becomes negligible in shaping the observable properties of the SN. This theoretical expectation is strongly supported by the distinct bimodal distribution observed in the M23 models (Fig. A4).

Given this fundamental limitation in detecting and characterizing low-mass CSM environments, we restrict our subsequent analysis of $R_{\rm CSM}$ to events where the predicted $M_{\rm CSM}$ exceeds $10^{-2.5}$ M$_\odot$.

Table A3. $M_{\rm CSM}$ and $R_{\rm CSM}$ coefficients.

|	C_0	C_1	C_2	C_3	C_4	C_5	C_6	C_7	C_8	C_9	C_{10}	C_{11}
$M_{\rm CSM} \leq 5$ d	−4.51	2.28	2.07	−0.24	1.07	−2.88	−0.19	0.0823	2.10	−1.24	−0.16	−12.35
$M_{\rm CSM} > 5$ d	−3.54	13.24	−3.85	5.94	0.22	−30.16	−9.55	−1.10	4.64	4.31	−2.26	42.92
$R_{\rm CSM} \leq 5$ d	0.65	0.43	−2.91	0.51	0.14	1.93	0.57	0.18	−1.04	0.039	−0.071	−10.05
$R_{\rm CSM} > 5$ d	−0.41	30.75	0.24	−4.57	0.29	5.67	5.47	−0.042	−4.65	−0.18	0.22	0.055
	C_{12}	C_{13}	C_{14}	C_{15}	C_{16}	C_{17}	C_{18}	C_{19}	C_{20}	C_{21}	C_{22}	C_{23}
$M_{\rm CSM} \leq 5$ d	−16.12	−2.31	5.66	2.76	−0.13	8.06	−2.24	2.19	0.84	−6.88	−3.95	0.20
$M_{\rm CSM} > 5$ d	5.95	1.44	10.72	−8.35	4.53	−29.78	5.17	3.19	−10.21	−42.38	7.66	−6.04
$R_{\rm CSM} \leq 5$ d	3.82	−0.16	3.71	−0.41	0.29	2.89	0.54	−0.46	−0.46	−1.03	5.83	−0.46
$R_{\rm CSM} > 5$ d	6.36	0.0098	−7.77	0.64	−0.49	−4.28	−0.59	0.22	−0.13	−93.03	−0.35	4.6
	C_{24}	C_{25}	C_{26}	C_{27}	C_{28}	C_{29}	C_{30}	C_{31}	C_{32}	C_{33}	C_{34}	C_{35}
$M_{\rm CSM} \leq 5$ d	5.85	0.085	−2.11	25.25	16.32	−5.72	−8.03	6.91	1.87	−2.97	−12.91	−2.31
$M_{\rm CSM} > 5$ d	61.57	9.91	−5.03	−86.78	−6.18	−10.02	29.54	45.11	−3.81	−31.43	43.9	−15.97
$R_{\rm CSM} \leq 5$ d	−3.99	−0.55	1.03	20.35	−3.84	−3.69	−2.94	0.77	−2.92	2.07	−10.30	−0.17
$R_{\rm CSM} > 5$ d	−11.87	−5.48	4.68	−0.54	−6.38	7.74	4.31	93.82	0.11	6.21	0.49	−31.53
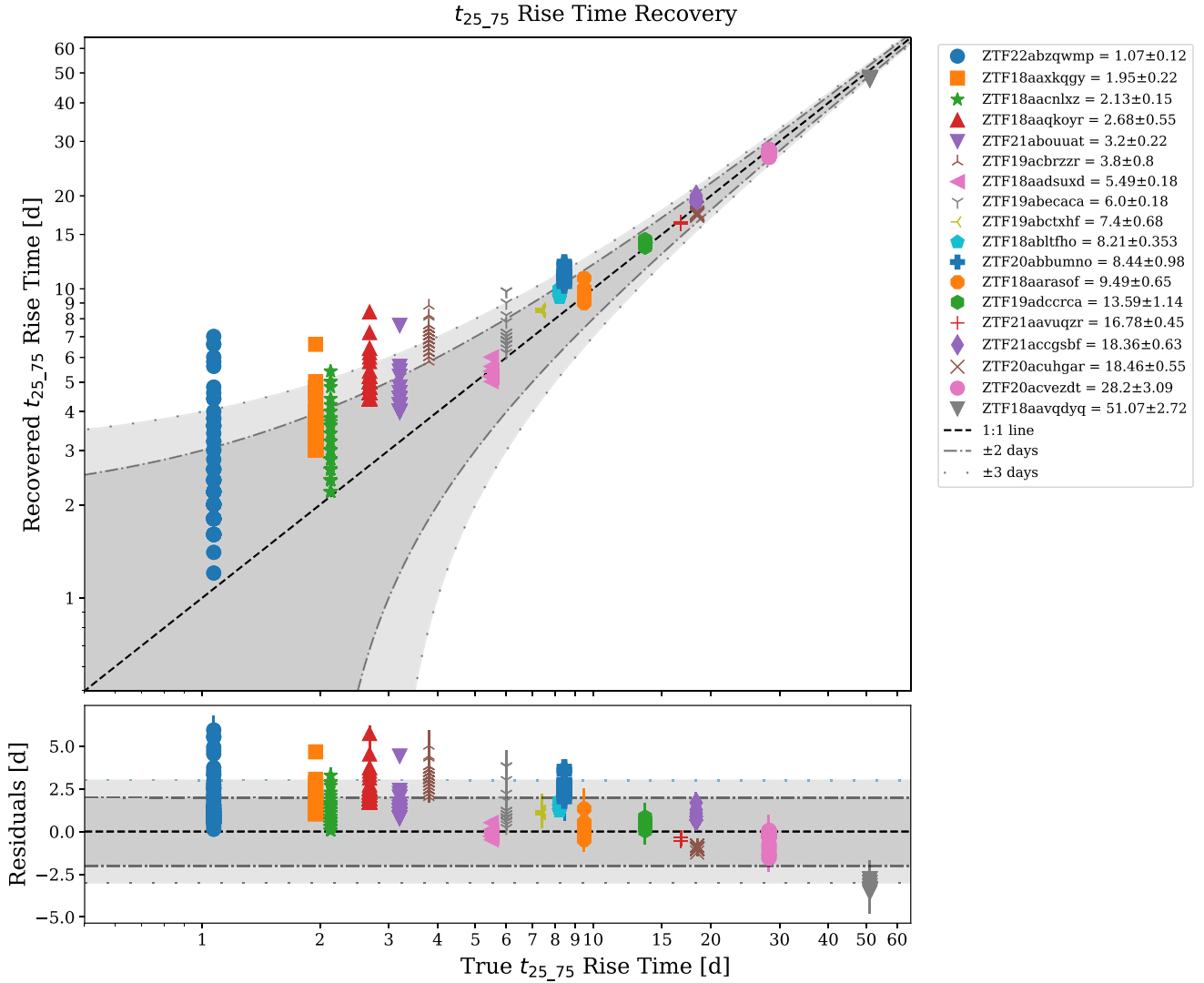
Figure A1. t_{25_75} rise time recovery exploring the impact of resampling high cadenced light curve (see in the legend) to the sampling function of less well-sampled light curves. The diagonal dashed line is the 1:1 line, the dot–dashed line encloses ± 2 d, and the dotted line encloses ± 3 d. The bottom plot shows the residual between the 'true' rise time of each event versus the measurements from resampling.

A10 Impact of systematic misclassifications

Most SN classifications from the BTS rely on the low-resolution SEDM spectrograph ($R \sim 100$). The limited spectral resolution and typically single-epoch observations near maximum light can make distinguishing certain SN subclasses challenging, particularly Type IIb from Type II and, to a lesser extent, Type IIn from Type II or host emission. Consequently, our Type II sample might contain some level of contamination from misclassified events, a consideration we quantitatively address here.

To quantify potential classification biases, we conducted Kolmogorov–Smirnov (KS) tests comparing Type II and Type IIb populations. KS tests of the unweighted $M_{g,\mathrm{peak}}$ and t_{25_75} distributions yielded p-values of 0.038 and 0.0030, respectively, indicating statistically significant differences between these populations. We identified an approximately 5 per cent shortfall of Type IIb SNe in our sample ($7.22^{+2.40}_{-1.84}$ per cent versus the expected $\sim$12.5 per cent from Shivvers et al.'s 2017 volume-complete sample). To assess the impact of possible misclassifications, we applied a conservative approach by removing the fastest-rising 5 per cent of Type II SNe – those most likely to be misclassified Type IIbs and have the largest impact on our results – and recalculated the M_{CSM} KDE distribution. The fraction of Type II SNe with $M_{\mathrm{CSM}} \geq 10^{-2.5}$ M$_\odot$ remained consistent (38–41 per cent) with our original finding ($\sim$36 per cent). This represents the most extreme scenario, confirming that potential misclassifications affect our results by less than 1σ.

Similarly, our analysis yields a Type IIn rate of $4.34^{+1.49}_{-1.09}$ per cent relative to Type II SNe, consistent with Shivvers et al. (2017). We consider the possibility of misclassification between regular Type II SNe and Type IIn events to be minimal for several reasons: (1) Type IIn SNe typically exhibit higher luminosities and represent a small fraction of the overall population, resulting in negligible statistical impact after V_{max} weighting; (2) BTS routinely conducts follow-up observations using higher resolution spectrographs for suspected Type IIn events to refine classification; and (3) wee see that <2 per cent of our Type IIn sample exhibits photometric characteristics resembling typical Type II events (e.g. $t_{25\_75} \leq 3$ d and $M_{g,\mathrm{peak}} > -18$ mag, which represent the median values for our unweighted Type
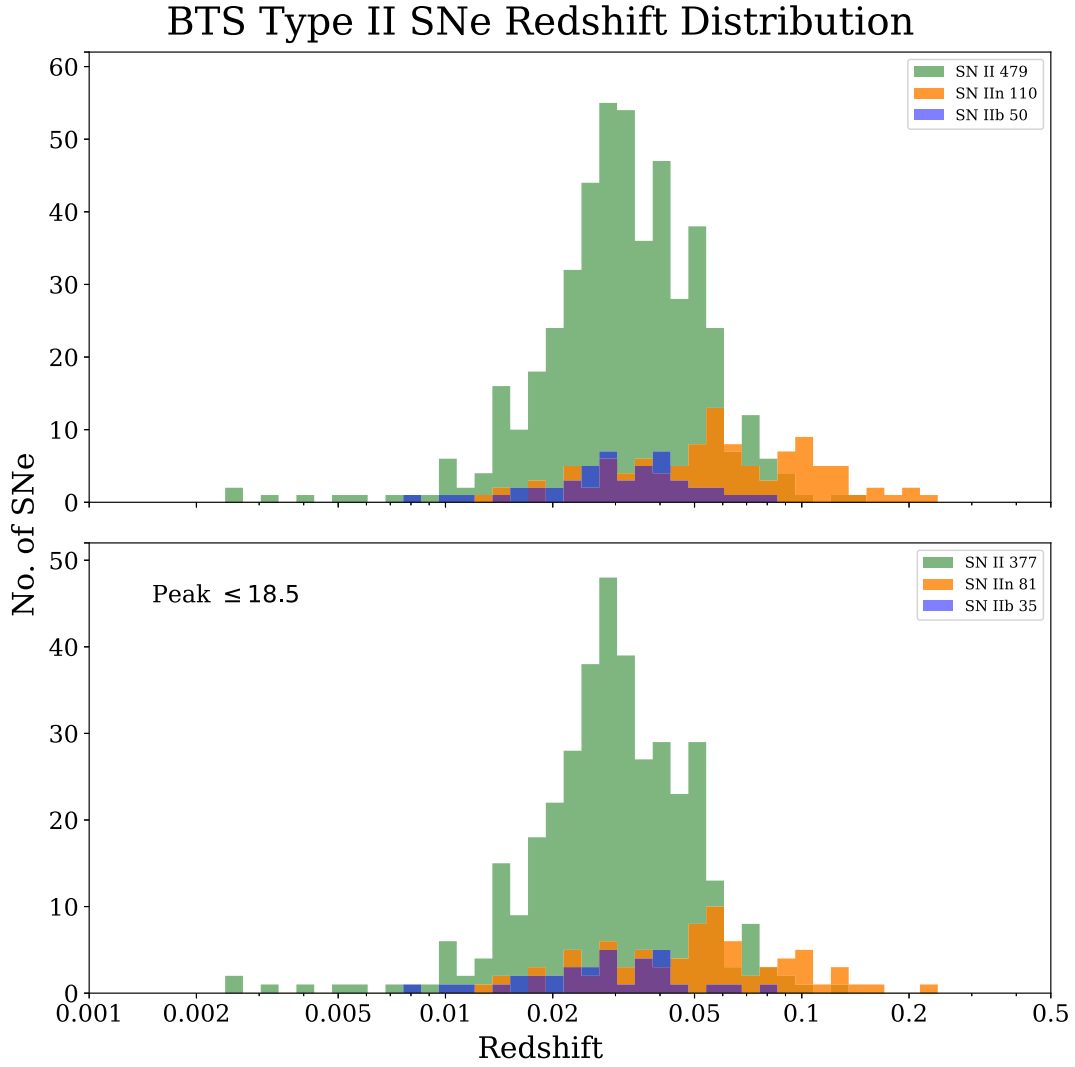
BTS Type II SNe Redshift Distribution

Figure A2. Distribution of redshift, z, across the for the whole sample (top) and for the sample with a $m_{peak} \leq 18.5$ mag (bottom).

II sample; Table 4). Our robust classification methodology ensures complete Type IIn identification, and our focus on CSM around fast-rising SNe means the longer evolution time-scales of Type IIn events minimally impact our conclusions.

We have also considered the potential impact of peculiar events resembling SN 1987A on our results. Such objects, characterized by moderate peak luminosities combined with unusually slow rise times (e.g. ZTF18acbwaxk), represent rare occurrences in the local universe. If several such events were misclassified or included within our sample, their statistical contribution would remain minimal given our V_{max} weighting and large sample size.
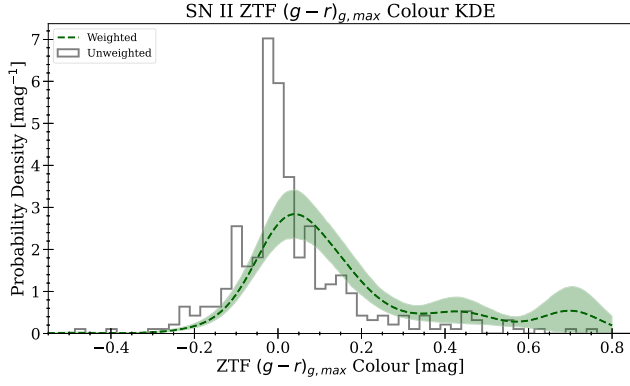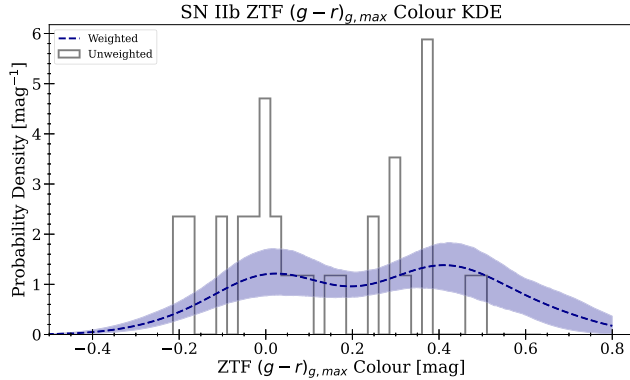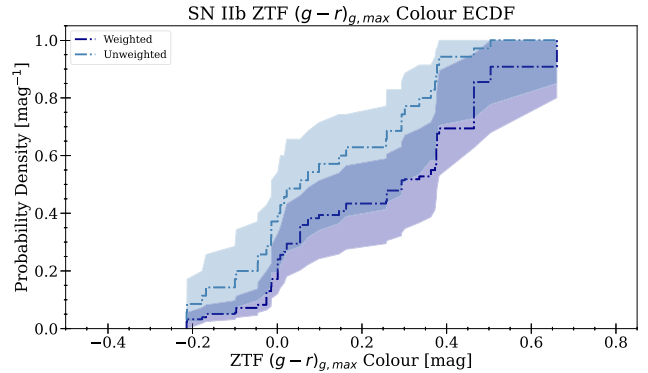
(a) Type II Peak Colour, $(g-r)_{g,max}$, KDE.
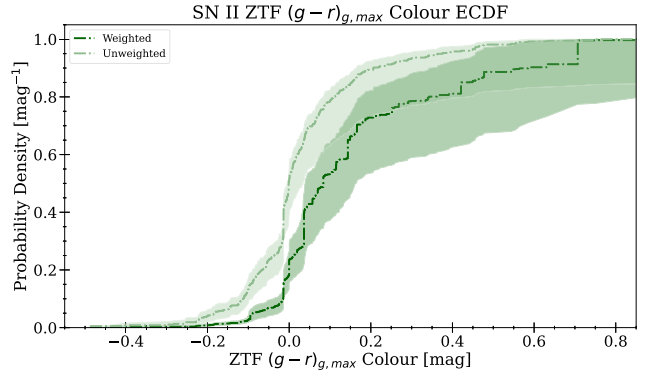
(b) Type II Peak Colour, $(g-r)_{g,max}$, ECDF.
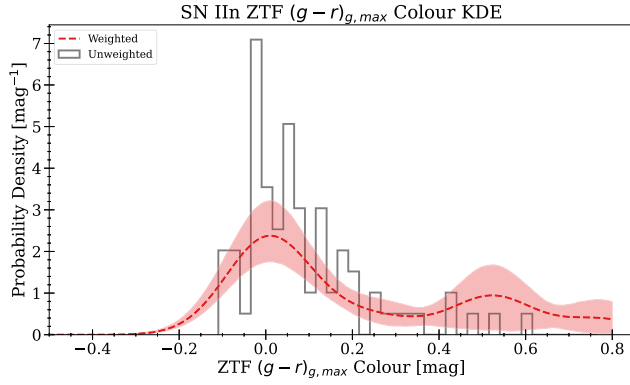
(c) Type IIn Peak Colour, $(g-r)_{g,max}$, KDE.
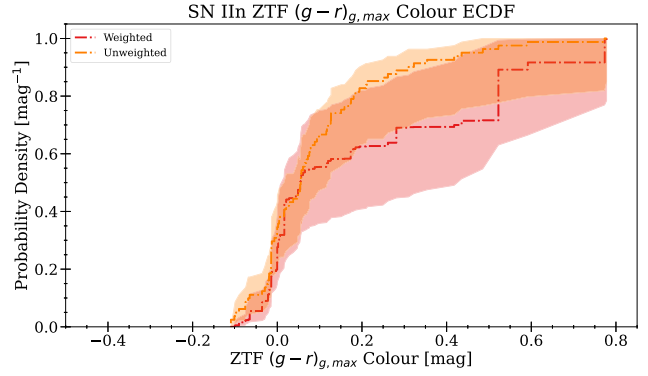
(d) Type IIn Peak Colour, $(g-r)_{g,max}$, ECDF.

(e) Type IIb Peak Colour, $(g-r)_{g,max}$, KDE.

(f) Type IIb Peak Colour, $(g-r)_{g,max}$, ECDF.

Figure A3. KDE (left) and ECDF (right) for Type II (top), Type IIn (middle), and Type IIb (bottom) showing the ZTF $g-r$ colour at ZTF g peak, $(g-r)_{g,\mathrm{max}}$, for the purposes of correcting for host extinction using the colour at peak. A correction, detailed if Section 2.4 is applied to events with a $g-r \geq 0.25$ mag and $t_{25\_75} < 20$ d.
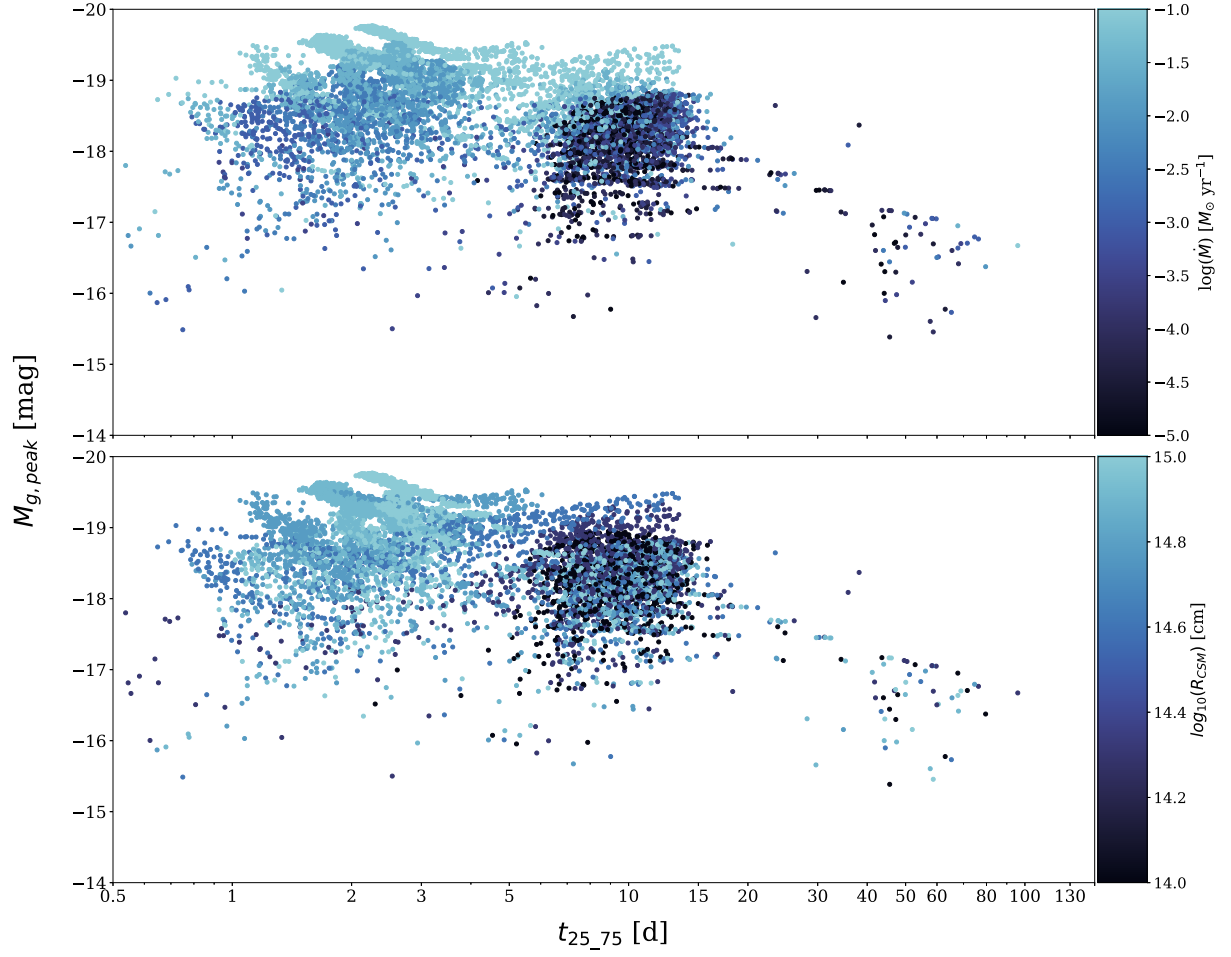
Figure A4. t_{25_75} versus $M_{g,\text{peak}}$ distribution for the theoretical light-curve grid from M23, with points drawn from a sample of 10 000 models, colour-coded by $\dot{M}$ (top) and $\log(R_{\text{CSM}})$ (bottom). The weighting is the same as applied in Fig. 8.
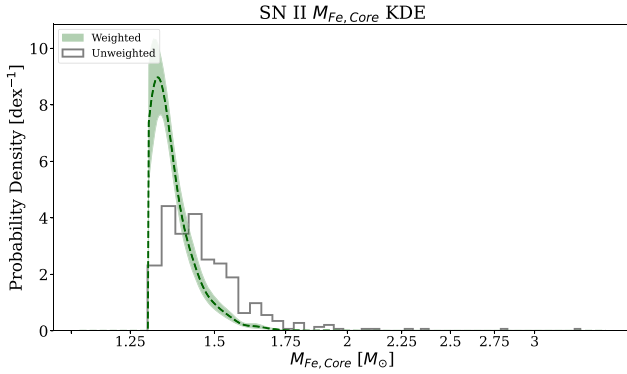

Figure A5. Type II KDE for $M_{\text{Fe,Core}}$ along with the associated 80 per cent CI. The weighted distribution is the dashed line (dark green) and the unweighted normalized histogram is the solid line (black).
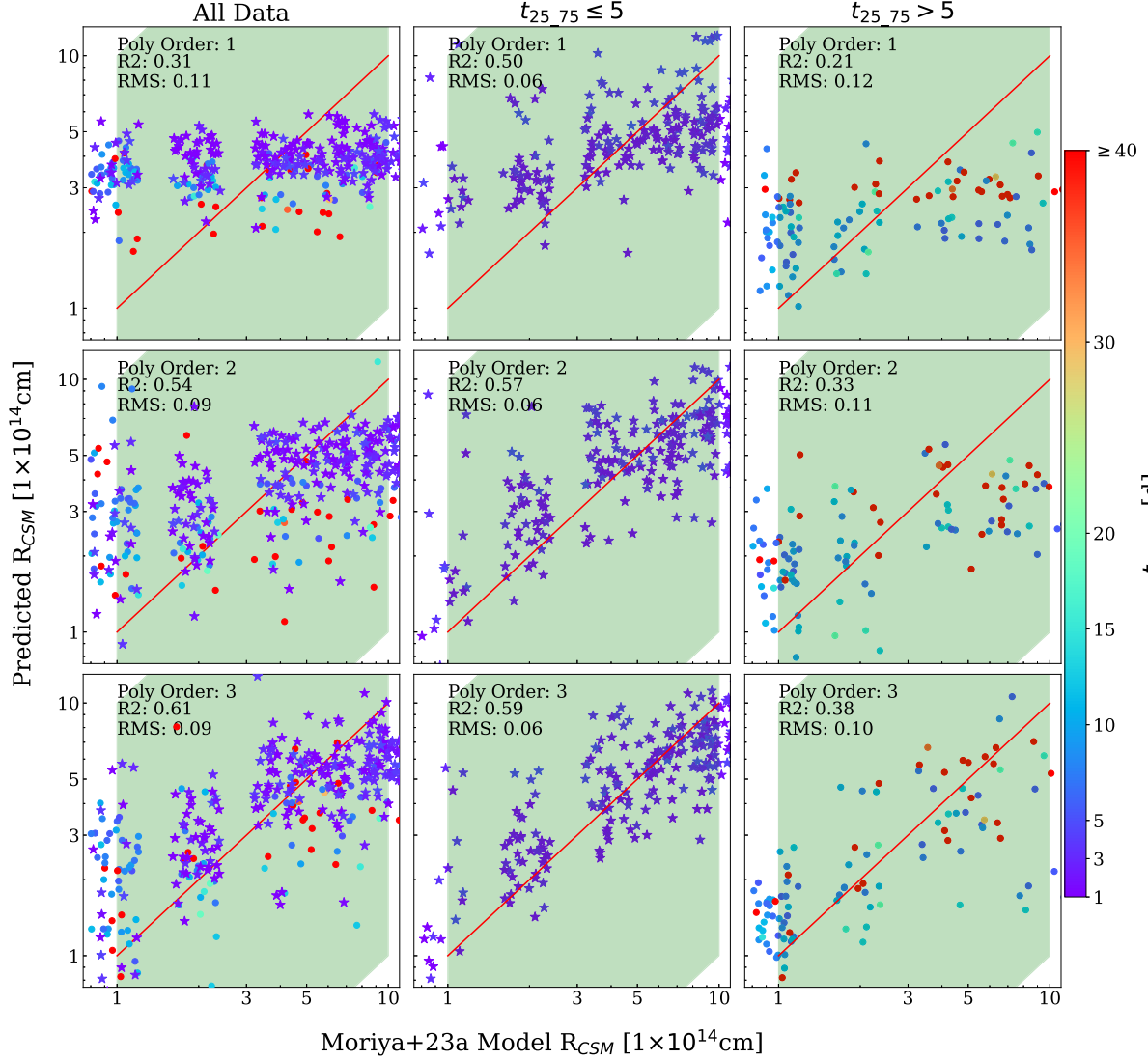
Figure A6. Multivariate analysis results of the predicted R_{CSM} radial extent (*y*-axis) versus the M23 R_{CSM} radial extent (*x*-axis). The top, middle, and bottom rows are polynomial orders 1, 2, and 3 respectively. The first column contains all the data and stars are those with $t_{25\_75} \le 5$ d with the second and 3third rows containing only data with $t_{25\_75} \le 5$ and > 5 d to show how the correlations predictive power decreases significantly for events with $t_{25\_75} \ge 5$ d. The diagonal (red) line is the 1:1 line with the (green) shaded region showing 1 order of magnitude above and below. This is run only on M23 models where $M_{CSM} \ge 1 \times 10^{-2.5}$ $M_\odot$ as we identify in Section 5.1 this to be the lower limit, above which $M_{g,peak}$ and t_{25_75} were influenced.
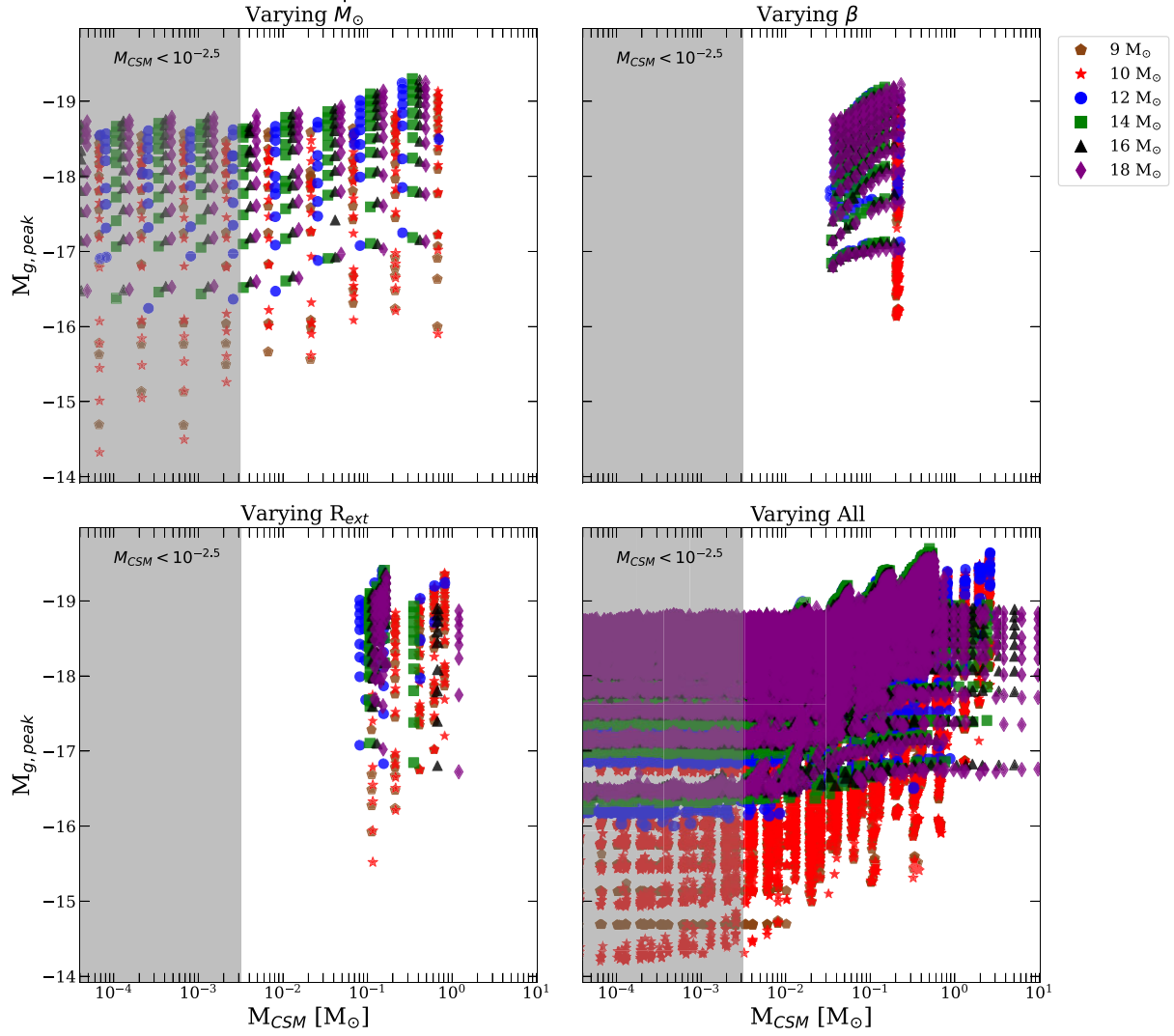
Figure A7. Dependence of $M_{g,peak}$ on M_{CSM} under different parameter variations, with fixed Ni mass and explosion energy. Top left – varying $\dot{M}$ with fixed β and R_{CSM}. Top right – varying β with fixed $\dot{M}$ and R_{CSM}. Bottom left – varying R_{CSM} with fixed $\dot{M}$ and β. Bottom right – combined variation of all CSM parameters ($\dot{M}$, β, and R_{CSM}). Each panel shows results for different progenitor masses (10—18 $M_\odot$). Below $M_{CSM} \approx 10^{-2.5}$ $M_\odot$, CSM properties do not significantly influence the peak magnitude, indicating a transition to CSM-negligible evolution.

This paper has been typeset from a TeX/LaTeX file prepared by the author.